

Magnetic field dependence of a Josephson traveling-wave parametric amplifier and integration into a high-field setup

L.M. Janssen¹, G. Butseraen^{2,3}, J. Krause¹, A. Coissard³, L. Planat³, N. Roch^{2,3},
G. Catelani^{4,5}, Yoichi Ando^{1,†} and C. Dickel^{1,*}


¹*Physics Institute II, University of Cologne, Zùlpicher Str. 77, Köln 50937, Germany*

²*Université Grenoble Alpes, CNRS, Grenoble INP, Institut Néel, Grenoble 38000, France*

³*Silent Waves, 25 Avenue des Martyrs, Grenoble 38000, France*

⁴*JARA Institute for Quantum Information (PGI-11), Forschungszentrum Jùlich, Jùlich 52425, Germany*

⁵*Quantum Research Center, Technology Innovation Institute, Abu Dhabi 9639, UAE*

 (Received 1 March 2024; revised 18 June 2024; accepted 4 October 2024; published 7 November 2024)

We investigate the effect of the magnetic field on a photonic crystal Josephson traveling-wave parametric amplifier (TWPA). We show that the observed change in the photonic band gap and plasma frequency of the TWPA can be modeled by considering the suppression of the critical current in the Josephson junctions (JJs) of the TWPA due to the Fraunhofer effect and closing of the superconducting gap. Accounting for the JJ geometry is crucial for understanding the field dependence. In one in-plane direction, the TWPA band gap can be shifted by 2 GHz using up to 60 mT of field, without losing gain or bandwidth, showing that TWPAs without superconducting quantum interference devices (SQUID) can be field tunable. In the other in-plane direction, the magnetic field is perpendicular to the larger side of the Josephson junctions, so the Fraunhofer effect has a smaller period. This larger side of the JJs is modulated to create the band gap. The field interacts more strongly with the larger junctions, and as a result, the TWPA band gap closes and reopens as the field increases, causing the TWPA to become severely compromised already at 2 mT. A slightly higher operating limit of 5 mT is found in the out-of-plane field, for which the TWPA's response is hysteretic. These measurements reveal the requirements for magnetic shielding needed to use TWPAs in experiments where high fields at the sample are required. With magnetic shields and at a distance from a sample at the magnet center, we can operate the TWPA while applying over 2 T to the sample.

DOI: [10.1103/PhysRevApplied.22.054018](https://doi.org/10.1103/PhysRevApplied.22.054018)

I. INTRODUCTION

Superconducting parametric amplifiers have become a key tool in quantum technology because they enable low-noise readout of weak microwave signals [1]. Nowadays, thanks to phase-matching techniques, Traveling-wave parametric amplifiers (TWPAs) can combine high gain, bandwidth, and saturation power [2–8], positioning themselves as ideal tools for scalable low-noise amplification. However, since most TWPAs depend on superconductivity, they face inherent problems in the presence of strong magnetic fields. This is particularly problematic because many experiments involving magnetic fields at the sample could benefit from or already rely on the low-noise amplification provided by TWPAs. These include superconducting qubit experiments [9–13], experiments with spin ensembles [14–16], spin qubits [17,18] or topological qubits [19], as well as hybrid setups including mechanical

[20,21] and magnonic degrees of freedom [22,23], and the search for axions [24,25]. While magnetic-field-resilient parametric amplifiers made from high-kinetic-inductance superconductors have been demonstrated recently [26–31], TWPAs resilient to magnetic fields are, to our knowledge, yet to be demonstrated. There are several recent experiments with magnetic fields at the sample that have utilized TWPAs (see, e.g., Refs. [15,19,24,25,32,33]), emphasizing the need for a comprehensive study of TWPAs in magnetic field.

Here we present measurements and a theoretical description of the effect of the magnetic field on a photonic crystal Josephson-junction (JJ) TWPA [3]. We estimate the maximum field that can be applied to the TWPA without compromising performance, giving an indication of the required magnetic shielding for a given stray field from the device under test. In the process, we show that the in-plane field along an appropriate direction can be a viable tuning knob to change the operating frequency of a TWPA without severely compromising performance. The tuning is a consequence of the suppression of the critical current of

*Contact author: dickel@ph2.uni-koeln.de

†Contact author: ando@ph2.uni-koeln.de

the individual JJs, which is due to the Fraunhofer effect and the suppression of the superconducting gap (see, e.g., Ref. [13]); the former is strongly dependent on JJ geometry. Because of the distinct values of the critical field and Fraunhofer period, we can tell the two contributions to the tuning of the JJs apart, which was difficult in previous experiments [10,13]. We also observe deviations from the commonly used Ginzburg-Landau (GL) formula for the gap suppression, deviations that are consistent with the predictions of Abrikosov-Gorkov (AG) theory [34,35] for pair breaking due to the magnetic field. In addition to the magnetic field dependence, we show that with several layers of magnetic shields, the TWPA can be operated at about a 40-cm distance from the magnet center in our setup with fields above 2 T at a device under test. We also establish an understanding of the operation of circuit quantum electrodynamics (cQED) and hybrid experiments in magnetic fields, e.g., if one wants to couple a JJ array to another system in the presence of small magnetic fields.

Two TWPAs are used in this work, each of the commercially available Argo model, made by Silent Waves. The data in Secs. I–III were measured on one such device, which we call TWPA A, while the data in Sec. IV were measured on a second TWPA, TWPA B. A detailed description and a summary of device parameters can be found in Appendix A. The circuit diagram and JJ geometry are shown in Figs. 1(a) and 1(b). The amplification is based on four-wave mixing, where two pump photons are converted to a signal and an idler photon via a nonlinear material—in this case a JJ transmission line. The JJs are made with the bridge-free double-shadow evaporation technique [36]. The JJ width w is designed to be the same for all JJs. The JJ geometry is varied by modulating the JJ height h , to engineer the dispersion relation, which is essential for increasing the gain and bandwidth of photonic crystal TWPAs. The JJ geometry is essential for modeling the experiment because one of the two ways a magnetic field can influence the Josephson inductance L_J is via the Fraunhofer effect. If a uniform current distribution is assumed, this effect modulates the inductance with a $1/|\text{sinc}(BA/\Phi_0)|$ dependence, where A is the area of the flux-penetrated region of the JJ, as shown in Fig. 1(b), and Φ_0 is the magnetic flux quantum. Our data show that not just the approximately 2-nm oxide barrier itself, but also some portion of the superconducting film on both sides is penetrated by the magnetic field, as expected because of the finite penetration depth for magnetic fields in a superconductor.

The transmission S_{21} of the TWPA without a pump and with an optimized pump are shown in Fig. 1(c). The measurement setup is described in Appendix B. The no-pump data show the photonic band gap at frequency f_g that results from the dispersion engineering. When a continuous microwave pump tone at the right frequency and power is applied, the transmission around the pump is enhanced

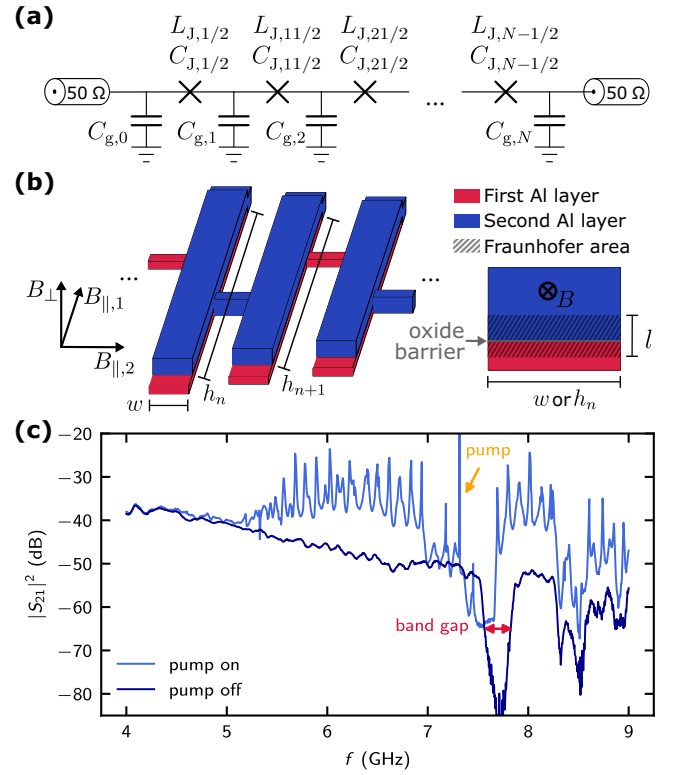


FIG. 1. (a) Schematic of the TWPA electrical circuit. The series of Josephson junctions (JJs) forms a nonlinear metamaterial. The Josephson inductances $L_{J,n}$, capacitances $C_{J,n}$, and ground capacitances $C_{g,n}$ are periodically modulated for dispersion engineering and chosen for impedance matching to 50 Ω . (b) Schematic of a part of the JJ array of the TWPA (not to scale). Two layers of aluminum with aluminum oxide junction barriers form a series of junctions. The width $w = 0.7 \mu\text{m}$ of these junctions is the same for all, while the height h is modulated by $\pm 5\%$ to engineer a photonic band gap (on average $h = 16 \mu\text{m}$). The field directions are named based on their orientation relative to the junction array. On the right, a cross section of the JJ area is shown to illustrate the Fraunhofer area in the case where the magnetic field penetrates the JJ. (c) TWPA transmission $|S_{21}|^2$ with the pump tone turned off and on. The gap feature of the TWPA is visible in both signals. From the pump-off data, we estimate the gap frequency f_g as the frequency of the $|S_{21}|^2$ minimum. The dips beyond 8 GHz are not a feature of the TWPA, but due to the circulators in the setup being out of specification.

due to the four-wave mixing, showing gain over a certain bandwidth on both sides of the band-gap feature. We focus on the gain below f_g , as in our setup f_g is close to the upper edge of the working frequency range of the circulators that were used.

II. TWPA OPERATION UNDER THE $B_{\parallel,1}$ FIELD

To understand the magnetic field dependence of the TWPA, we start with the $B_{\parallel,1}$ direction [as defined in Fig. 1(b)]. In Fig. 2, the transmission through the TWPA

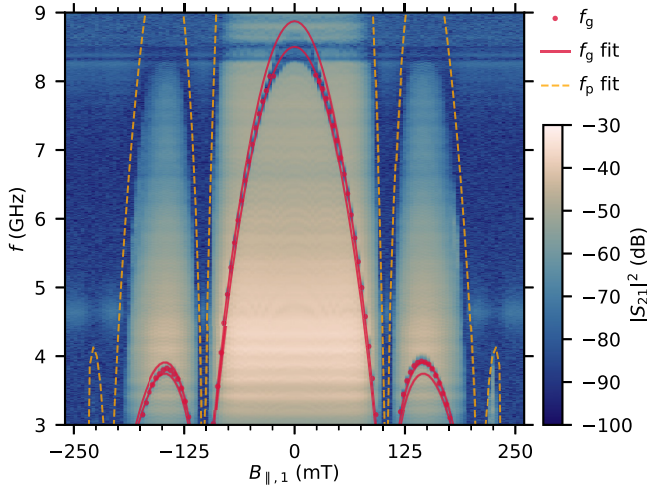


FIG. 2. TWPA transmission spectrum $|S_{21}|^2$ without pump tone as a function $B_{\parallel,1}$. The gap frequency f_g is estimated by the $|S_{21}|^2$ minimum and data points with $f_g < 8$ GHz are shown and used in the fit (red dots). Above 8 GHz the circulators are out of specifications, causing additional features in the data and making the f_g estimate less reliable. The upper and lower edges of the gap are calculated from our model, and shown as solid red lines. The best fit is obtained by taking the average of these two and fitting this to the measured f_g . The plasma frequency f_p , based on the same model, is plotted as an orange dashed line.

for a range of field values $B_{\parallel,1}$ is plotted. The two distinctive features of the TWPA transmission are the frequency of the band gap f_g and the plasma frequency f_p , where the transmission is cut off. A Fraunhofer pattern is clearly visible for both. The gap frequency f_g , as marked by the red dots, is estimated by the frequency of the $|S_{21}|^2$ minimum, and is only plotted in the region where the band gap does not overlap with the circulator features above 8 GHz, which make the $|S_{21}|^2$ minimum unreliable. For an unknown reason, f_g is slightly different for positive and negative magnetic fields, and the second Fraunhofer lobe appears more strongly for the positive field direction. Hysteresis was considered as the possible reason, but we see the same result independent of the sweep direction. Therefore we are only able to fit the data accurately for one side.

Starting from the circuit model described in Ref. [3], we can calculate f_g and f_p for each field value. The TWPA is a transmission line made of JJs and capacitances to ground, as illustrated in Fig. 1(a). The JJs can be modeled with a Josephson inductance $L_{J,n+1/2}$ and capacitance $C_{J,n+1/2}$, both of which depend on the junction area. The Josephson inductance is inversely proportional to the critical current, which is in turn proportional to the area. The Josephson capacitance is simply proportional to the area. Thus, the modulation of h leads to a modulation of the inductance $L_{J,n+1/2}$, capacitance $C_{J,n+1/2}$, and the capacitance to ground $C_{g,n}$ where index n denotes the position in the JJ array. The capacitance to ground $C_{g,n}$ of each island

is achieved by covering the entire JJ array with a dielectric and depositing a thick copper ground plane on top. Since the area of an island is almost entirely determined by the area of the junctions, we assume the same modulation for $C_{g,n}$ as for $C_{J,n+1/2}$.

The combination of the modulation of $L_{J,n+1/2}$, $C_{J,n+1/2}$, and $C_{g,n}$ causes a photonic band gap that is used for phase matching the TWPA. From this circuit model, one can calculate an effective impedance Z for the TWPA, as well as f_g and f_p . To calculate the magnetic field dependence of the TWPA transmission and the parameters mentioned above, we need to model the magnetic field dependence of $L_{J,n+1/2}$.

We consider that the magnetic field affects the JJs by suppressing the superconducting gap Δ according to AG theory and through the Fraunhofer effect. We assume that the capacitances $C_{J,n+1/2}$ and $C_{g,n}$ are unaffected by the magnetic field. The Josephson inductances are inversely proportional to the gap: $L_{J,n+1/2} \propto 1/\Delta(B_{\parallel,1})$. For the Fraunhofer dependence, the geometry matters. The Fraunhofer effect arises from an interplay of the JJ current and the magnetic field. The most straightforward assumption would be a rectangular current distribution in each junction. However, we find that parametrizing the current distribution to allow for more current density at the edges of the junctions gives a better fit. It is certainly possible that the oxide barrier is slightly thinner away from the center of the junctions, which could mean that the actual current distribution is indeed closer to the one we use for fitting. The field $B_{\parallel,1}$ is in plane with respect to the junction array and perpendicular to the narrow side of the junctions of width w . Since w is unchanged throughout the array, the suppression of the critical current is identical for all junctions. This significantly simplifies the magnetic field modeling: instead of applying a change to each junction individually, we only need to change the average Josephson inductance \bar{L}_J .

The full model can be found in Appendix C; the best fit obtained using Eqs. (C6), (C8), and (C11), and using as fit parameters the field $B_{\Phi,1}$ corresponding to a flux quantum through area A , the average Josephson inductance at zero field \bar{L}_J , and the parameter governing the current distribution χ , is shown in Fig. 2. The critical field B_c is not used as a fit parameter because it can be read off directly from the data. For the fit, the extracted f_g around zero field were ignored, specifically those fitted to be larger than 8.1 GHz. When the gap frequency is above this threshold, the minimum of $|S_{21}|^2$ is likely a bad estimate for f_g due to the circulators being out of band. As the model also suggests, the magnetic field changes the TWPA impedance, such that at the Fraunhofer minimum $|S_{21}|^2$ breaks down because the TWPA becomes reflective, which is supported by $|S_{11}|^2$ measurements (see Appendix D). The features of the measured plasma frequency are reproduced accurately. The fact that the second Fraunhofer lobe is reproduced

indicates that we have a good understanding of the field dependence of the superconducting gap.

After understanding the effect of the magnetic field based on the pump-off transmission data and circuit model, we now proceed to look at how the amplifier figures of merit, in particular the gain and bandwidth, change with $B_{\parallel,1}$ for the TWPA pumped with a microwave tone of frequency f_{pump} and power P_{pump} . We did not measure the added noise of the TWPA as a function of the magnetic field, as the measurements would have taken significantly longer and extracting the absolute added noise would have required additional calibration measurements of the setup. However, the TWPA was factory characterized and we measure similar gain in the setup; thus, we can estimate the added noise at zero field (see Appendix E). An example of the TWPA gain profile is shown in Fig. 3(a). We estimate the gain profile not by subtracting the pump-off transmission, but rather by estimating a field-independent background without the band gap (see Appendix E for details on the background subtraction). The gain profile shows strong fluctuations that depend on f_{pump} and P_{pump} . In an actual experiment, if one wants to optimize the amplifier gain at a particular frequency, f_{pump} and P_{pump} can be optimized to give the best signal-to-noise ratio (SNR) at that particular frequency. We have instead decided to smooth the gain profile with a 500-MHz window filter and optimized on the maximum smooth gain [see Fig. 3(a)]. The bandwidth of the smoothed gain is also shown as a figure of merit, but not used for the optimization of the pump tone. This figure of merit is somewhat arbitrary but convenient, as the smoothed gain landscape allows for the extraction of a meaningful bandwidth and we found that the optimization landscape is relatively well behaved, giving consistent optima when running the optimization from different starting conditions.

We have tuned up the TWPA at different fields by optimizing the maximum smooth gain, varying f_{pump} and P_{pump} as free parameters using the Nelder-Mead method [37]. Figures 3(b) and 3(c) show the resulting gain and bandwidth. More details on the optimization and other figures of merit are reported in Appendix E. We see that the maximum smooth gain remains stable up to $B_{\parallel,1} = 60$ mT, although the maximum gain does decrease. Additionally, the bandwidth of the gain does not decrease significantly up to this field. However, the frequency range where amplification occurs is shifted by 2 GHz. This shows that an in-plane field in this specific direction can be used to effectively tune the amplification range of the TWPA across a wide range.

III. TWPA OPERATION FOR OTHER FIELD DIRECTIONS

In this section, we show how the TWPA responds to magnetic fields applied in the other principal field

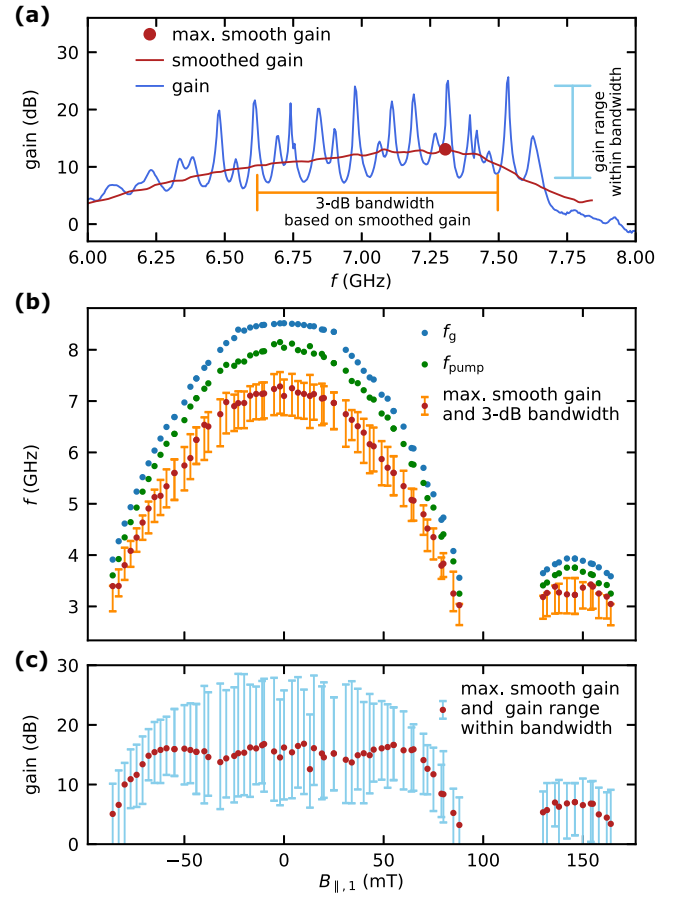


FIG. 3. (a) TWPA gain as a function of the frequency. All gain curves are calculated relative to a fixed background estimate, not to the pump-off spectrum. To obtain figures of merit that are robust to the gain ripples, we smooth the gain as a function of the frequency and use the maximum of the smoothed gain and the 3-dB bandwidth based on the smoothed gain. (b) Frequency of the maximum smoothed gain and bandwidth window as a function of $B_{\parallel,1}$. The TWPA band-gap feature can be tuned by about 2 GHz with the in-plane field, while the optimum gain remains roughly stable, then the gain becomes compromised. (c) Maximum smooth gain and gain range within the 3-dB-bandwidth window as a function of $B_{\parallel,1}$. While the highest gain values are continuously reduced with $B_{\parallel,1}$, the maximum smooth gain remains stable up to about $|B_{\parallel,1}| < 60$ mT.

directions $B_{\parallel,2}$ and B_{\perp} , as indicated in Fig. 1(b), starting with $B_{\parallel,2}$. The pump-off TWPA transmissions as a function of $B_{\parallel,2}$ are shown in Fig. 4(a). There is a Fraunhofer pattern similar to Fig. 2, but with a much smaller period, indicating a lower B_{Φ} . Specifically, we find that $B_{\Phi,2} = 4.55$ mT, whereas $B_{\Phi,1} = 107.8$ mT. This is in line with the TWPA dimensions, as $h/w = 22.7$, which is similar to $107.8 \text{ mT} / 4.55 \text{ mT} = 23.7$. This shows that both datasets imply the thickness of the field-penetrated area l [see Fig. 1(b)] to be the same, namely, 28.5 nm. This value for l is reasonable since it should be compared to

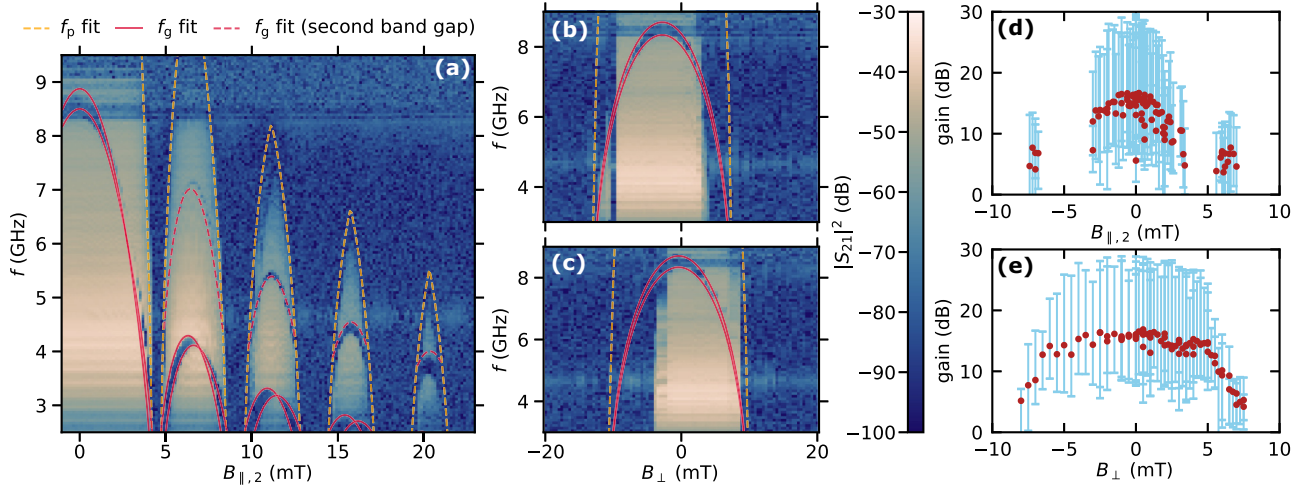


FIG. 4. (a) TWPA transmission spectrum without pump tone as a function of $B_{\parallel,2}$. The edges of the fitted first band gap f_g are shown as red lines. The corresponding f_p is shown as an orange dashed line. The fitted center of the second band gap is indicated with a dashed red line. Note that these lines are not fitted to the data shown here. Instead, the model parameters are the same as in Fig. 2, except for the field corresponding to a flux quantum, as the flux now penetrates the longer side of the junction. To account for this, the value of the flux quantum was modified based on the geometry of the junctions, yielding the curves shown here. (b),(c) No-pump TWPA transmission spectrum as a function of B_{\perp} , scanning in the negative and positive directions, respectively. Here too, f_p and f_g are shown, fitted with a GL-like phenomenological formula (see Appendix C 4). The hysteresis is much larger than for the in-plane directions. (d),(e) Optimized maximum smooth gain and gain range as a function of $B_{\parallel,2}$ and B_{\perp} , respectively.

roughly half of the total thickness of the two aluminum layers forming the JJs [38].

There are striking qualitative differences between the dependence on $B_{\parallel,2}$ and on $B_{\parallel,1}$. In Fig. 4(a), we observe a periodic closing and reopening of the band gap. This is due to the interplay between the modulation of h , which creates the band gap, and the Fraunhofer effect. In the $B_{\parallel,1}$ direction, w is nominally identical for all JJs, so we should obtain the same Fraunhofer dependence for all JJs, resulting in a common prefactor for all $L_{J,n+1/2}$ (assuming perfectly identical geometries), as mentioned previously. But, in the $B_{\parallel,2}$ direction, the different h_n result in different Fraunhofer contributions: the Fraunhofer critical current modulation has a smaller period for JJs with larger h than for JJs with smaller h . However, the JJs with large h had lower L_J to begin with. As a result, the difference between the L_J values for the different junctions decreases initially with increasing field, and at some point, this effectively cancels out the modulation of the capacitances $C_{J,n+1/2}$ (which remains constant with field) and closes the band gap. More details on this modeling, based on the same combination of AG gap suppression and Fraunhofer effect as for $B_{\parallel,1}$, can be found in Appendix C 2. We also see higher harmonics of the band gap in the Fraunhofer side lobes, that are not there for the $B_{\parallel,1}$ direction. Lastly, there is a line of low transmission with a large upward slope in the second side lobe starting around 10 mT, but we do not understand this feature.

The B_{\perp} field dependence [see Fig. 4(b) for sweeping B_{\perp} in the negative direction and Fig. 4(c) for the positive sweep direction] is different from the in-plane directions. Here, we initially observe a decrease of f_g , but the transmission then suddenly breaks down. We see strong hysteresis in the sweep direction: the maximum of f_g is offset by 2.4 mT. This is in strong contrast to the $B_{\parallel,1}$ and $B_{\parallel,2}$ directions, where we estimate the hysteresis to be less than 1 mT. The hysteresis could be due to Abrikosov vortices that an out-of-plane field can create in superconducting films. The vortices can lead to increased inductance because of the associated currents, but they will also increase dissipation. We estimate a critical field $B_{c,\perp} = 10.3$ mT based on the f_g dependence. The ratio of the in-plane and out-of-plane critical fields is $B_{c,\perp}/B_{c,\parallel} \simeq 0.04$, which is reasonable for thin-film aluminum. A quantitative understanding of vortices in the JJ array is beyond the scope of this work. More details on the B_{\perp} direction can be found in Appendix C 4.

We compare the optimized gain as a function of $B_{\parallel,2}$ and B_{\perp} in Figs. 4(d) and 4(e). Notably, the gain collapses for $B_{\parallel,2}$ and B_{\perp} at 2 and 5 mT, respectively, while it is stable up to 60 mT for $B_{\parallel,1}$. This means that the Fraunhofer dependence for the large JJ direction is imposing the strongest field limit on TWPA performance, but the limits due to vortices and gap suppression in B_{\perp} are of the same order of magnitude. The gain and bandwidth for all three different field directions as a function of the estimated f_g are also discussed in Appendix E.

IV. SHIELDED TWPA OPERATION

From the previous measurements, one can estimate the magnetic shielding required to operate a TWPA in a dilution refrigerator with strong magnetic fields at the device under test. The cryostat used in this experiment features a 6 T/1 T/1 T vector magnet. If the TWPA is mounted on the mixing chamber stage, the stray fields at 6 T will be of the order of 30 mT, which is incompatible with TWPA operation. The magnetic shielding needs to keep the field at the TWPA below 1 mT. For TPWAs with superconducting quantum interference devices (SQUIDs), the shielding requirements are likely more stringent, because the SQUID periods are often chosen to be of the order of 100 μ T. A strong magnet that is not operated in persistent-current mode can also lead to considerable low-frequency noise [13] that would likely compromise a SQUID-based TWPA. To shield the TWPA from magnetic fields, a superconductor is a clear candidate material. Aluminum was readily available, and its low critical temperature means that it can easily be heated out of the superconducting state and cooled back down again at zero field to regain shielding after being compromised by a field exceeding its critical field. However, the critical field of aluminum is not high enough to withstand the large stray field of the vector magnet. To mitigate this, outer shields of a high-permeability material can be used. In this experiment, Cryoperm was used, which is a material similar to mu-metal, but designed to perform at cryogenic temperatures. The shield setup is described in detail in Appendix F, and shown in Fig. 13 therein.

To test the magnetic shields, we measured the transmission through the TWPA and also the optimized gain as a function of the field at the magnet center. If the shielding setup were perfect, no change in the transmission or gain would be observed. We optimized the gain at zero field and ramped both 1-T coils (B_x and B_y in the magnet coordinate system) of the vector magnet to the maximum and saw no change in f_g or in the gain. However, the shields are not sufficient to fully shield the stray fields of the 6-T magnet B_z , which likely saturates the Cryoperm shield that also leads to the failure of the superconducting aluminum shield. As shown in Fig. 5(a), when the magnet is ramped above 2.5 T, enough stray field penetrates the shields to change f_g and quickly suppress the gain [Fig. 5(a)]. Additionally, we observe ripples in the transmission that become stronger with the field. These ripples are not constant in frequency and we believe them to be a response of the TWPA to low-frequency noise related to the magnet, possibly due to vibrations of the TWPA relative to the magnet. For the dataset in Fig. 5, we did not optimize the pump settings and ramped back down from 6 T to see if the gain would recover, which it did [see Fig. 5(b)].

A wide range scan from 6 to -6 T and additional details can be found in Appendix F. There we show that we can

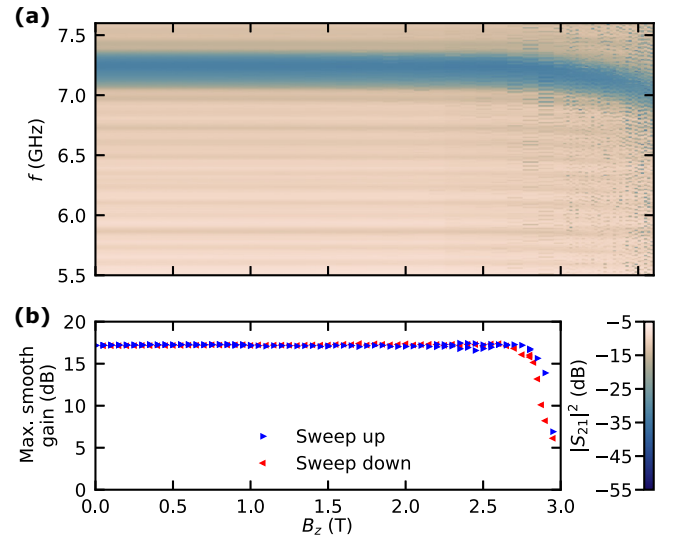


FIG. 5. (a) No-pump transmission of the shielded TWPA as a function of the magnetic field at the magnet center. Up to about 2.5 T, not much changes, but for higher fields, the band gap is tuned down and there is additional noise that manifests at dips in the signal. (b) Maximum smooth gain as a function of the magnetic field. Here the gain was optimized at zero field and settings were not updated at every field. Around 2.5 T the gain changes and is strongly reduced by 3 T.

still get high gain at fields up to 3.5 T, but only by running the gain optimization procedure again: since f_g shifts, the pump settings need to be adjusted. Between 4 and 5 T, the TWPA transmission eventually breaks down, showing that the shielding can still be improved. However, sweeping the magnet back down, TWPA transmission is restored with a slight shift in f_g . We confirmed that a thermal cycle above 1.5 K can reset the device and the shielding capabilities, showing that the shields are not permanently compromised. To have more flexibility and be able to measure even with a compromised TWPA, we installed cryogenic switches that allow bypassing the TWPA (see Appendix F).

To use the TWPA with higher fields at the sample, one could either improve the shielding or increase the distance between the TWPA and magnet. In our case, the magnet is below the mixing chamber and we simply mounted the shielded TWPA above at a distance of about 40 cm from the magnet center. While one could mount the TWPA higher up and still attach it to the mixing chamber, we investigated the temperature dependence of the TWPA's performance to explore the possibility of mounting it at a higher stage of the dilution refrigerator (see Appendix G). We only measured the gain and transmission and found no change in performance up to about 0.3 K. While we did not perform detailed measurements of the added noise as a function of temperature, our data would suggest that mounting the TWPA at the cold plate ($T \approx 0.1$ K) is a viable option. Another option would be the installation of

a compensation coil at the TWPA. Such a setup has been shown to allow operation at higher fields [25].

V. CONCLUSION

In conclusion, we characterized the magnetic field dependence of a Josephson junction TWPA and found that it strongly depends on field direction. The in-plane magnetic field along the direction perpendicular to the junction array can be an option for tuning the frequency of the amplification band of a JJ TWPA down by 2 GHz at similar gain and bandwidth with fields up to 60 mT. At 60 mT, the saturation power is reduced by about 10 dB. Magnetic field tuning of a TWPA with 100- μ T out-of-plane fields has been shown previously in TPWAs with SQUIDS [3]. The in-plane field is an interesting alternative as the field required for tuning is about 2 orders of magnitude larger. Hence, a similar level of flux noise would lead to less added noise. Similar ideas for the tuning of JJ arrays, but not in the context of parametric amplifiers, have been reported in Ref. [39]. At the same time, a few millitesla of the out-of-plane field or in-plane field along the JJ array can severely compromise the TWPA. We can model the TWPA in-plane field dependence based on the magnetic field dependence of the JJ inductances due to the Fraunhofer effect and the suppression of the superconducting gap. This suggests that field dependence can be a diagnostic tool for extracting the parameters of the underlying circuit from the model, as the field does not affect the capacitances. However, we did not measure explicitly how the added noise of the TWPA changes with the field, as those measurements would have taken significantly longer. Understanding critical current noise introduced by noise in the magnetic field and possible noise from vortices are interesting future directions.

With magnetic shields and about a 40-cm distance between the TWPA and magnet center, we show that we can operate the TWPA at more than 2 T at the magnet center. From about 2.5 T we observe additional noise in the TWPA transmission. Between 4 and 5 T, stray fields break superconductivity in the TWPA, but after sweeping the field back down and thermal cycling the TWPA recovers. We also implemented cryo-switches to bypass the TWPA, realizing a versatile test setup for cQED experiments at high magnetic field with a near-quantum-limited amplifier.

The setup was controlled based on [QCoDeS](#) drivers and logging [40]. The measurements were run using [Quantify-core](#) [41].

Datasets and analysis in the form of Jupyter notebooks that create the figures are available from Zenodo [42].

ACKNOWLEDGMENTS

We thank Timur Zent for making the CAD drawings of the magnetic shields and helping with the assembly

of the cryogenic setup. We thank Arno Bargerboos for his advice and for sharing his experience with TPWAs in magnetic shields. We thank Tom Paquin from MuShield for competent advice on magnetic shields as well as speedy delivery. We thank Daniel Strange and Riccardo Vianna from Oxford Instruments for sharing detailed data on the stray field of our magnet. This project has received funding from the European Research Council (ERC) under the European Union's Horizon 2020 research and innovation program (Grant Agreement No. 741121) and was also funded by the Deutsche Forschungsgemeinschaft (DFG, German Research Foundation) under CRC 1238 - 277146847 (Subproject B01) as well as under Germany's Excellence Strategy - Cluster of Excellence Matter and Light for Quantum Computing (ML4Q) EXC 2004/1 - 390534769. This project has received funding from the European Union's Horizon Europe 2021-2027 project TruePA (Grant Agreement No. 101080152)

The project was conceived by C.D. and Y.A. in coordination with L.P. The TPWAs were fabricated by A.C. and L.P. and factory characterized by G.B., A.C., and L.P. The measurements were performed by L.M.J. and C.D. with help from J.K. and advice from G.B. and L.P. L.M.J. and C.D. built the setup for the TWPA in the fridge with the magnet with magnetic shields and bypass switches. The data were analyzed by L.M.J. and C.D. with help from G.B., N.R., and G.C. G.C. provided theory support for the project. The manuscript was written by L.M.J. and C.D. with input from all coauthors.

APPENDIX A: DEVICE DESCRIPTIONS

The TPWAs in this work are of the Argo model, commercially available and made by Silent Waves. The field dependence with the TWPA at the magnet center is measured on TWPA A, while the shield performance and the temperature dependence are measured on TWPA B. The TPWAs are fabricated and packaged by Silent Waves and delivered as a module with SMA connectors. The two TPWAs are similar to that described in Ref. [3], but have single JJs instead of SQUIDS. The JJs are fabricated using double-angle evaporation with a bridge-free design [36]. The film thicknesses of the first and second aluminum layers are 20 and 50 nm, respectively. The ground plane is made of a thick copper layer, so there are no large extended aluminum areas. Detailed parameters for both devices can be found in Table I.

Silent Waves measured the TWPA figures of merit in their setup before shipping. Electrical losses in the TWPA, a combination of insertion loss and loss within the TWPA, were estimated to be 4–5 dB in the factory calibration. These losses have to be offset by the gain to improve performance. The factory calibration estimated an SNR improvement of 6 dB for a gain similar to that measured in this work.

TABLE I. Parameters of the two TWPAs in this work. Parameters are used in the modeling.

Device	L_J (pH)	C_g (fF)	C_J (fF)	w (μm)	\bar{h} (μm)	η (%)	N_J	N_p	f_g (GHz)
TWPA A	95	38	500	0.7	16	± 5	1596	28	8.7
TWPA B	133	29	490	0.7	16	± 5	1800	33	7.2

APPENDIX B: MEASUREMENT SETUP FOR MAGNETIC FIELD DEPENDENCE

The measurement setup for the magnetic field dependence of the TWPA is illustrated in Fig. 6. In the course of previous experiments [13], it was observed that the Quin-star circulators with a double layer of magnetic shielding at their positions above the mixing chamber plate behave normally up to about 2 T at the magnet center, so they are not expected to affect the measurements of the TWPA inside the magnet. The TWPA experiments were performed with the device in the puck of a bottom-loading dilution refrigerator (Triton 500, Oxford Instruments) with a nominal base temperature of about 10 mK. A three-axis 6 T/1 T/1 T vector magnet was used to apply magnetic fields to the sample. In this paper, we do not perform field cooling of the TWPA, but we change the magnetic field while keeping the device at base temperature. During the cooldown, the magnet was shorted and disconnected from its power supply to avoid the creation of vortices during the superconducting transition of the TWPA. For the $B_{||,1}$ axis, we mainly used the Oxford Instruments Mercury iPS power supply, which can supply sufficient current

to reach a magnetic field of 1 T. For the other two axes, we used a Keithley 2461 SourceMeter as a current source that can only reach magnetic fields of 0.16 T, but is more fine grained and less noisy. For all measurements of the shielded setup, the Mercury iPS was used for all field directions, so we could see the shield performance with up to 6 T of magnetic field at the sample.

The alignment of the magnet axes was such that B_x , B_y , B_z , correspond to B_\perp , $B_{\parallel,1}$, $B_{\parallel,2}$. We took angular scans of the magnetic field at fixed $|B|$ to estimate the degree of misalignment, but in particular for the B_\perp direction, the hysteresis is more significant than any potential misalignment. Misalignment is likely less than 1° .

The TWPA transmission and gain measurements were performed with a vector network analyzer (VNA), and an additional microwave source was used as a pump. The wiring was such that we could use a room-temperature microwave switch to measure the TWPA in reflection or transmission and to also reverse the pump direction (see the wiring diagram shown in Fig. 6). We use 60 dB of attenuation in the input lines to ensure that the TWPA input noise is low, but we do not use Eccosorb or other filters here that would avoid pair-breaking radiation. For operating the TWPA in an actual experiment, a directional coupler would be used to couple in the pump tone, but to just measure the TWPA itself, this is not necessary. The fridge wiring is not entirely optimal for the TWPA, as the band gap is slightly above 8 GHz, outside the specifications of the circulators that were mounted in the fridge. For the mounting of the TWPA in the fridge with shields, wider range circulators were used (see Appendix F).

APPENDIX C: TWPA MODEL

Here we present the model for the TWPA with the modulation in the junction dimension h ; see Fig. 1(b). The model is based on that of Ref. [3] and is used to derive formulas for the plasma and band-gap frequencies that can be directly compared with experiment. The model also returns the effective impedance of the array, which can be used to understand the reflection at the input and output. In the first part of this appendix, we focus on the effect of field $B_{\parallel,1}$. The other in-plane field direction is treated in Appendix C2. Appendix C3 concerns the suppression of the superconducting gap by the field, and Appendix. C4 considers the perpendicular field.

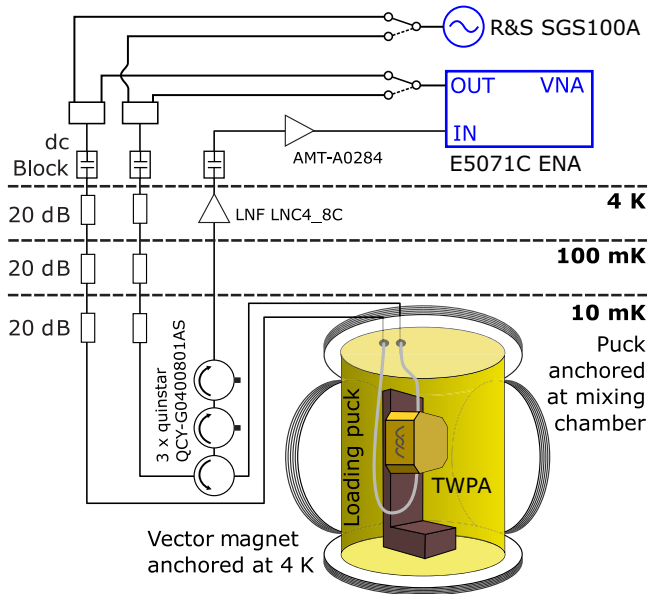


FIG. 6. Wiring diagram and setup for the measurements with the TWPA inside the puck. The TWPA is mounted roughly at the center of the vector magnet and the field dependence is studied. Both reflection and transmission measurements were possible.

The phase matching of the TWPA is achieved by periodic modulation of the Josephson inductance and capacitance, by varying the size of the junctions. Let N_J be the number of junctions in the TWPA. Then we have $N_J + 1$ superconducting islands, which we index with integers $n = 0, 1, \dots, N_J$. We index the Josephson junction between two islands with half-integers: the junction between islands n and $n + 1$ is indexed $n + 1/2$. Since the modulation of the Josephson junctions is periodic, we can define the entire array using a small set of parameters. Let \bar{L}_J and \bar{C}_J be the average Josephson inductance and capacitance, respectively, and let \bar{C}_g be the average capacitance to ground of an island. We denote by N_p the period of the modulation and by η the junction area modulation amplitude. Then we have, for any island n and any junction $n + 1/2$,

$$L_{J,n+1/2}^{-1} = \bar{L}_J^{-1} \{1 + \eta \cos[G(n + 1/2)]\}, \quad (C1)$$

$$C_{J,n+1/2} = \bar{C}_J \{1 + \eta \cos[G(n + 1/2)]\}, \quad (C2)$$

$$C_{g,n} = \bar{C}_g \left\{ 1 + \frac{\eta}{2} \sum_{\pm} \cos \left[G \left(n \pm \frac{1}{2} \right) \right] \right\}, \quad (C3)$$

where $G = 2\pi/N_p$. Note that the modulation amplitude of the junction area determines the modulation of L_J , C_J , and C_g . For L_J and C_J , this is clear: these are inversely proportional and proportional to the junction area, respectively. The ground capacitance C_g is proportional to the area of the islands because it is achieved using a single ground plane on top of the entire junction array. Then the modulation of C_g follows from the geometry of the device, as each island consists of two junction areas, and a negligible area connecting the two junction areas [see Fig. 1(b)]. Hence, the modulation amplitude of the area of an island is the same as that of the junctions, but we need to average the modulation of two junctions.

We first consider the plasma frequency f_p , above which transmission through the TWPA is strongly suppressed. For any junction, it is given by $\omega_p = 1/\sqrt{\bar{L}_{J,n+1/2} \bar{C}_{J,n+1/2}}$. Note that the modulation cancels so that at zero field we get the same plasma frequency for each junction:

$$\omega_p(0) = 1/\sqrt{\bar{L}_J \bar{C}_J}. \quad (C4)$$

In general, the Josephson inductance L_J is related to the critical current I_c of a JJ via $\bar{L}_J = \Phi_0/(2\pi I_c)$, where Φ_0 is the superconducting flux quantum and I_c is proportional to the superconducting gap Δ and the junction's conductance. An in-plane magnetic field is perpendicular to the current flow in the tunnel barrier, so we expect a Fraunhofer pattern in the critical current I_c . Additionally, the superconducting gap is suppressed with field, causing a

decrease in I_c (the gap suppression is discussed in more detail in Appendix C3). Therefore, we model the in-plane field dependence of the critical current as

$$I_c(B) = I_{c,0} |\text{sinc}(\pi \phi / \Phi_0)| [\Delta(B/B_c)/\Delta_0], \quad (C5)$$

where $I_{c,0}$ and Δ_0 denote quantities in zero field, $\phi = BA$ with A the area penetrated by flux [cf. Fig. 1(b)], $\text{sinc}(x) = \sin(x)/x$, and B_c is an appropriately chosen critical field.

1. $B_{\parallel,1}$ direction

For the $B_{\parallel,1}$ magnetic field direction, the Fraunhofer-type modulation of I_c is identical for all junctions in the array because the field is applied perpendicular to w , the dimension of the Josephson junction that is not modulated. As such, we can apply Eq. (C5) to \bar{L}_J , rather than separately to each junction. Therefore,

$$\omega_p(B_{\parallel,1}) = \omega_p(0) \sqrt{\left| \text{sinc} \left(\pi \frac{B_{\parallel,1}}{B_{\Phi,1}} \right) \right| \frac{\Delta(B_{\parallel,1}/B_c)}{\Delta_0}} \quad (C6)$$

with $B_{\Phi,1} = \Phi_0/(lw)$.

The Fraunhofer pattern depends on the junction geometry as well as on the spatial distribution of the current through the junction. In particular, the sinc functional dependence is derived for a rectangular junction with uniform current. In Ref. [43], a one-parameter phenomenological model was proposed (and compared to experiment) for a rectangular junction that can interpolate between uniform current and current concentrated at the edges of the junction. We assume the current density profile

$$J = J_{\max} \frac{\cosh(2x\chi/L)}{\cosh(\chi)}, \quad (C7)$$

where L is the size of the junction (either h or w) and $x \in [-0.5L, 0.5L]$. The uniform current case is recovered in the limit $\chi \rightarrow 0$. For increasing χ , the current density in the interior decreases, while the edges stay at J_{\max} . The corresponding Fraunhofer pattern amounts to the substitution

$$\text{sinc } y \rightarrow \mathcal{F}(y, \chi) \equiv \frac{\chi^2}{\chi^2 + y^2} \left[\frac{y \sin y}{\chi \tanh \chi} + \cos y \right] \quad (C8)$$

in Eq. (C6).

We now turn to the calculation of the band gap in the low-power limit. In this regime, to calculate the edges of the band gap, we can use the linearized version of a set of equations found in Appendix B of Ref. [3] relating amplitudes A and B of waves with wave vectors k and $k - G$ and

frequency ω :

$$\left[\frac{\omega^2}{\omega_p^2 \ell_s^2} - k^2 \left(1 - \frac{\omega^2}{\omega_p^2} \right) \right] A \quad (C9)$$

$$+ \left[\frac{\eta}{2} \frac{\omega^2}{\omega_p^2 \ell_s^2} + \frac{\eta}{2} k(G-k) \left(1 - \frac{\omega^2}{\omega_p^2} \right) \right] B = 0,$$

$$\left[\frac{\eta}{2} \frac{\omega^2}{\omega_p^2 \ell_s^2} + \frac{\eta}{2} k(G-k) \left(1 - \frac{\omega^2}{\omega_p^2} \right) \right] A$$

$$+ \left[\frac{\omega^2}{\omega_p^2 \ell_s^2} - (G-k)^2 \left(1 - \frac{\omega^2}{\omega_p^2} \right) \right] B = 0. \quad (C10)$$

Here ℓ_s is the Coulomb screening length, $\ell_s = \sqrt{\bar{C}_J/\bar{C}_g}$. For $\eta = 0$ (no modulation), the two equations are decoupled and give degenerate solutions for $k = G/2$ (that is, at the band edge), and for $\eta > 0$, a band gap opens at $k = G/2$ (see, for example, Fig. 1 of Ref. [3]). Therefore, by finding the frequencies for which the wave with $k = G/2$ propagates, we find the frequencies of the edges of the band gap. Setting $k = G/2$ and the determinant of the system to zero, we find the values of ω for which this system has a nontrivial solution:

$$\omega_{g,\pm} = \omega_p \sqrt{\frac{(G/2)^2(1 \pm \eta/2)}{(G/2)^2(1 \pm \eta/2) + 1/\ell_s^2(1 \mp \eta/2)}}. \quad (C11)$$

The prefactor ω_p on the right-hand side should be understood to depend on the magnetic field as in Eq. (C6).

With this formula, we can fit the experimental data. As shown in Fig. 2, the center of the gap is extracted for each field value where the gap is visible. We can take the average of the frequencies found with Eq. (C11) and run a least-squares fitting procedure, where we vary $\omega_p(0)$, χ , and $B_{\Phi,1}$. For the other parameters, we use the designed values of TWPA A (see Table I). With this model, we cannot fit \bar{C}_J and \bar{C}_g independently, since they enter into the formula for the band gap through their ratio (in ℓ_s) and through $\omega_p(0)$ (which also depends on the Josephson inductance). The critical field B_c can be estimated directly from the data, considering the value at which transmission becomes undetectable, so we use the value $B_c = 236$ mT. Now we can fit the parameters mentioned:

$$f_p(0) = 23.0 \text{ GHz}, \quad \chi = 0.668, \quad B_{\Phi,1} = 107.8 \text{ mT}.$$

2. $B_{\parallel,2}$ direction

For the $B_{\parallel,2}$ direction, due to the modulation in the dimension h of the junctions normal to the field [cf. Fig. 1(b)], we have to modify the above results to take into account the fact that the Fraunhofer effect modulates the

Josephson inductance of the different junctions by different amounts. Considering junction $n + 1/2$, its inductance and capacitance are [cf. Eqs. (C1) and (C2)]

$$L_{J,n+1/2}^{-1} = \bar{L}^{-1} \{1 + \eta \cos[G(n + 1/2)]\} \left| \text{sinc} \left(\pi \frac{B_{\parallel,2}}{B_{\Phi,2}^{(n)}} \right) \right|, \quad (C12)$$

$$C_{J,n+1/2} = \bar{C} \{1 + \eta \cos[G(n + 1/2)]\}, \quad (C13)$$

with

$$B_{\Phi,2}^{(j)} = \bar{B}_{\Phi,2} / \{1 + \eta \cos[G(n + 1/2)]\}, \quad (C14)$$

where, based on the junction geometry (see Table I), we can relate $\bar{B}_{\Phi,2}$ to $B_{\Phi,1}$:

$$\bar{B}_{\Phi,2} = (0.7/16) B_{\Phi,1}. \quad (C15)$$

In practice, we treat $B_{\Phi,2}$ as a fit parameter and then check for consistency with the expectation from this equation; we find a discrepancy of order 4%; see Sec. III. This small difference might effectively account for the possibly different current distributions in the two directions, which are not known (in other words, the χ values, which, for simplicity, we assume to be identical, could, in fact, differ for the two directions).

In writing Eq. (C12) we assume that $B_{\parallel,2} \ll B_c$, so we can ignore gap suppression for simplicity; it can be straightforwardly included by multiplying the right-hand side of Eq. (C12) by $\Delta(B_{\parallel,2}/B_c)/\Delta_0$ [see Eq. (C5)]. The measurable plasma frequency is then given by the smallest one at the given field:

$$\omega_p(B_{\parallel,2}) = \min_{\{n\}} \left[\frac{1}{\sqrt{L_{J,n+1/2} C_{J,n+1/2}}} \right]$$

$$= \min_{\{n\}} \left[\omega_p(0) \sqrt{\left| \text{sinc} \left(\pi \frac{B_{\parallel,2}}{B_{\Phi,2}^{(n)}} \right) \right| \frac{\Delta(B_{\parallel,2}/B_c)}{\Delta_0}} \right]. \quad (C16)$$

For the band gap, assuming that $\eta \ll 1$ and $\eta \pi B_{\parallel,2}/\bar{B}_{\Phi} \lesssim 1$, we can find a simple generalization of Eq. (C11) as follows: we expand Eq. (C12) to first order in η and cast the result in a form similar to Eq. (C12) itself,

$$L_{J,n+1/2}^{-1} \simeq \bar{L}^{-1} \{1 + \beta \eta \cos[G(n + 1/2)]\} \left| \text{sinc} \left(\pi \frac{B_{\parallel,2}}{\bar{B}_{\Phi,2}} \right) \right| \quad (C17)$$

with the field-dependent factor

$$\beta = \pi \frac{B_{\parallel,2}}{\bar{B}_{\Phi,2}} \cot \left(\pi \frac{B_{\parallel,2}}{\bar{B}_{\Phi,2}} \right) \quad (C18)$$

or, if we use the current distribution assumption leading to the substitution in Eq. (C8),

$$\beta = \left[\frac{y \sin y}{\chi \tanh \chi} \left(y \cot y + \frac{2\chi^2}{\chi^2 + y^2} \right) + \cos y \left(1 - y \tan y - \frac{2y^2}{\chi^2 + y^2} \right) \right] \times \left(\frac{y \sin y}{\chi \tanh \chi} + \cos y \right)^{-1}, \quad (\text{C19})$$

where $y = \pi B_{\parallel,2}/\bar{B}_{\Phi,2}$. Then repeating the procedure used to arrive at Eq. (C11), we find that the expression for the band gap has the same form as in that equation if we replace $\eta \rightarrow \beta\eta$ in the numerator and

$$\omega_p \rightarrow \omega_p(0) \sqrt{\left| \text{sinc} \left(\pi \frac{B_{\parallel,2}}{\bar{B}_{\Phi,2}} \right) \right| \frac{\Delta(B_{\parallel,2}/B_c)}{\Delta_0}} \quad (\text{C20})$$

in the prefactor.

The field values $B_{\parallel,2}^{(n)}$ at which the band gap closes can be found by requiring $\omega_+ = \omega_-$, which leads to the condition

$$\beta = \frac{(G/2)^2 - 1/\ell_s^2}{(G/2)^2 + 1/\ell_s^2} \equiv \beta_c. \quad (\text{C21})$$

This should be contrasted with the condition $\beta = 0$ that corresponds to the (approximate) suppression of the spatial modulation of the Josephson inductance (or critical current). However, with our parameters we have $\beta_c \simeq -0.716$ and an approximate solution to Eq. (C21), when using Eq. (C18) for β , is

$$B_{\parallel,2}^{(n)} \simeq \bar{B}_{\Phi,2} \left[\left(n + \frac{1}{2} \right) - \frac{\beta_c}{\pi^2(n + 1/2)} \right], \quad n = 0, 1, \dots \quad (\text{C22})$$

The first term on the right-hand side satisfies the condition $\beta = 0$; the correction—that is, the second term—becomes smaller (and the approximation more accurate) as n increases.

Finally, we note that an approximate position for the center ω_c of the band gap is found by setting $\eta = 0$ in Eq. (C11), $\omega_c = \omega_p G/2 \sqrt{(G/2)^2 + 1/\ell_s^2}$. This formula can be easily generalized to estimate the position of the next band gap by replacing $G \rightarrow 2G$; cf. Fig. 4(a).

3. Field dependence of the superconducting gap for the in-plane field

Here we consider the dependence of the gap on the parallel magnetic field. Such a field can suppress superconductivity through two mechanisms: the Zeeman splitting of the electrons forming a Cooper pair, and the so-called

orbital effect—the suppression of the order parameter by the supercurrent that arises to screen the applied magnetic field. In films thin compared to the penetration depth, $t \ll \lambda$, the screening of the field can be ignored, but not the effect of the supercurrent on the order parameter. Whether the Zeeman effect plays a significant role or not depends on the dimensionless parameter

$$c = \frac{D(et)^2 \Delta_0}{6\hbar\mu_B^2} f(\ell/t), \quad (\text{C23})$$

where D is the electron diffusion constant, ℓ is the mean free path, and μ_B is the Bohr magneton [44]. The dimensionless function in the last factor has the limits $f(0) = 1$ and $f(x) \simeq 3/4x$ for $x \gg 1$. When $c > 1$, the order parameter suppression is dominated by the orbital effect and the Zeeman splitting can be ignored. Experimentally, it was found that $c \sim 1$ for films with $t \sim 7\text{--}8$ nm [45,46]. Given the rapid increase of c with thickness, even for the thinnest film forming the Josephson junctions, $t \simeq 20$ nm, the Zeeman effect plays only a negligible role. On the other hand, we note that the thicker film, $t \simeq 50$ nm, is still thinner than the penetration depth in Al films of this thickness, $\lambda > 100$ nm [47].

Having to consider only the orbital effect simplifies the calculation of the order parameter suppression, which is analogous to that due to paramagnetic impurities, as studied by Abrikosov and Gorkov [34,35]. At low temperatures $T \ll T_c$, we can use the $T = 0$ expressions up to exponentially small corrections that we ignore. The amount of gap suppression is determined by a dimensionless pair-breaking parameter α that in the present case can be written as $\alpha = (B/B_c)^2$, where B_c is the parallel critical field (in the notation of Ref. [35] we have the relation $\Gamma = \alpha \Delta_0/2$, where Γ is their dimensionful pair-breaking parameter). While the implicit transcendental equation determining Δ as a function of α has a relatively simple form amenable to straightforward numerical solution [see Eq. (3.5) of Ref. [35]], no closed-form solution is available. Here we propose a formula that interpolates between the analytically tractable limits $\alpha \rightarrow 0$ and $\alpha \rightarrow 1$, the latter value representing the critical one at which superconductivity disappears:

$$\Delta(\alpha) = \Delta_0 \sqrt{1 - \frac{\pi}{4}\alpha - \left(1 - \frac{\pi}{4}\right)\alpha^\gamma} \quad (\text{C24})$$

with $\gamma = (12 - \pi)/(4 - \pi) \simeq 10.32$. As shown in Fig. 7 this formula is a good approximation to the numerically exact solution, deviating less than 2% from the latter.

Note that, due to the large exponent γ , the last term under the square root in Eq. (C24) can be dropped if α is not too close to unity; even with this additional approximation the deviation from numerics remains below 2% for

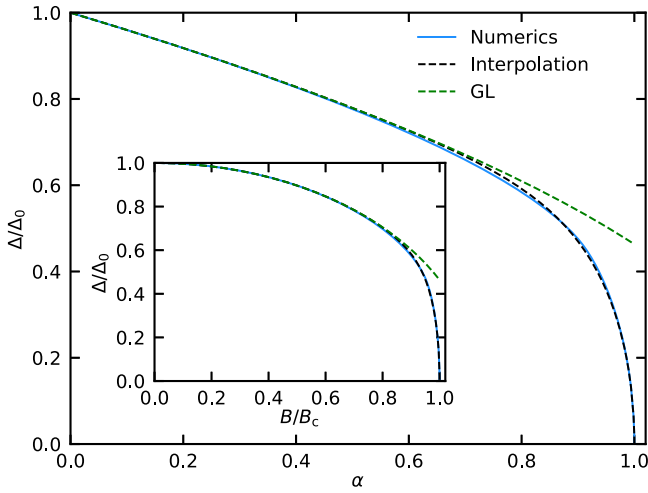


FIG. 7. Normalized order parameter as a function of the pair-breaking parameter $\alpha = (B/B_c)^2$. Solid blue line represents the numerical solution to the equation of Ref. [35] determining the gap suppression at zero temperature within AG theory. Black dashed line represents the analytical interpolation, Eq. (C24). Green dashed line represents the GL-type approximation; cf. Eq. (C25). Inset: same as the main panel, but plotted as a function of the parallel magnetic field normalized by the critical one.

$\alpha \lesssim 0.7$, corresponding to $B/B_c \lesssim 0.84$ (see the inset of Fig. 7). In this range, we can therefore write

$$\Delta(B/B_c) \simeq \Delta_0 \sqrt{1 - \left(\frac{B}{\tilde{B}_c}\right)^2}, \quad (\text{C25})$$

where $\tilde{B}_c = 2B_c/\sqrt{\pi} \simeq 1.128B_c$. This shows that up to fields not too close to the critical one, the gap suppression (at zero temperature) takes the form familiar from Ginzburg-Landau theory [valid near the critical temperature; see Eq. (4.52) of Ref. [48]], although the effective critical field \tilde{B}_c entering this expression overestimates the actual critical field B_c by almost 13%.

Given the above discussion of the approximate expression in Eq. (C25), one may wonder if the data can be satisfactorily fitted just by using the Ginzburg-Landau formula shown there. However, setting the critical field to the measured value cannot reproduce the f_p of the second Fraunhofer lobe accurately; see Fig. 8(a). The thin-film AG gap dependence fits f_p more accurately because Δ remains higher and is then more quickly suppressed when increasing the field towards the critical one, as seen in Fig. 8(b). On the other hand, the band-gap frequency f_g can be fitted as accurately with the GL formula as with the AG one because we cannot measure it as close to B_c and we can use the additional fit parameter χ to adjust the curve. In both cases, we need to assume a higher current density at the edges of the JJs, but to perform the fitting with the GL expression, we need to assume a less uniform current density than for the AG case; see Fig. 8(c).

Based on the model we can also estimate the TWPA impedance Z as a function of the field; see Figs. 8(d) and 8(e). The impedance of the array is equal to $Z = \sqrt{\tilde{L}_J/\tilde{C}_g}$. The capacitance to ground \tilde{C}_g does not change with magnetic field, and we obtain a value for \tilde{L}_J at any magnetic field from the fit. Therefore we can calculate Z at any value of $B_{\parallel,1}$. At zero field we find that the TWPA is well matched to $50\ \Omega$, but the tuning of f_g with $B_{\parallel,1}$ is accompanied by an increasing impedance, which diverges as the field approaches a Fraunhofer minimum. Therefore, the insertion loss at the TWPA grows, showing that tunability by field in the TWPA would always come at the cost of some reduction in performance.

4. B_{\perp} direction

Here we briefly discuss some aspects of the TWPA behavior in the perpendicular field. In Figs. 4(c) and 4(d) we see that the field where the breakdown in $|S_{21}|^2$ occurs varies by scan direction, but f_g is also tuned down with B_{\perp} . We can try to estimate $B_{c,\perp}$ by fitting the f_g dependence. The dependence of f_g , suggests a GL-like expression [cf. Eq. (C25)] of the form

$$f_g(B) = f_g(0) \sqrt{1 - \left(\frac{B_{\perp} - B_{\text{offset}}}{B_{c,\perp}}\right)^2} \quad (\text{C26})$$

for the band-gap edges with a different B_{offset} for the two sweep directions. We do not consider a Fraunhofer contribution in this direction as the field is parallel to the JJ current. This model can describe the data reasonably well for a plausible $B_{c,\perp} = 10.3\ \text{mT}$, which is also consistent with the breakdown in $|S_{21}|^2$ [vertical dashed lines in Figs. 4(b) and 4(c)]. The critical field $B_{c,\perp}$ can be related to the coherence length ξ by [48]

$$B_{c,\perp} = \frac{\Phi_0}{2\pi\xi^2}, \quad (\text{C27})$$

which gives $\xi \simeq 180\ \text{nm}$. Also, the ratio between $B_{c,\perp}$ and the parallel critical field $B_{c,\parallel}$ for thin films depends on the film thickness t as [48]

$$\frac{B_{c,\perp}}{B_{c,\parallel}} = \frac{t}{2\sqrt{3}\xi}. \quad (\text{C28})$$

From this expression and the measured critical fields, we would estimate $t \simeq 27\ \text{nm}$, within a factor of 2 from the thickness of the thicker film (which has a lower critical field compared to the thinner one).

Finally, let us consider the question of hysteresis, which we assume is due to the presence of at least one stable vortex in some of the junctions. For a superconducting strip of

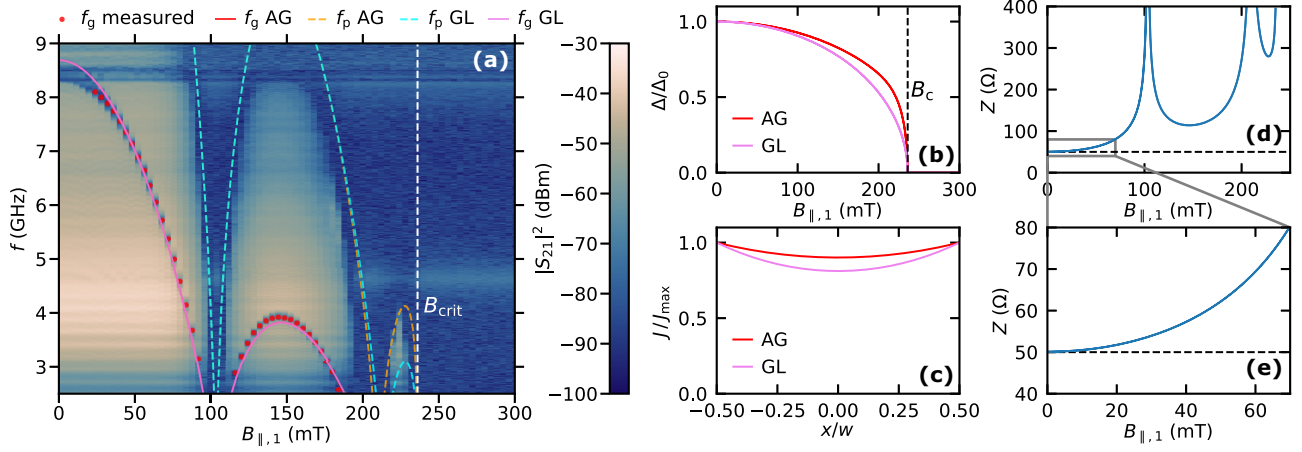


FIG. 8. Details on the $B_{\parallel,1}$ dependence of the pump-off TWPA transmission. (a) TWPA transmission spectrum without the pump tone as a function of $B_{\parallel,1}$, the same as in Fig. 2(a). It shows the same fit for f_g and f_p based on the AG model, and a fit using GL dependence for Δ for comparison. The fits overlap for low fields because away from B_c the difference in $\Delta(B)$ [see (b)] can be compensated by adapting the current distribution in the model [see (c)]; however, only the AG fit can accurately capture the second Fraunhofer lobe. (d),(e) Impedance of the TWPA junction array as a function of the field. While the junction array is impedance matched to the environment at zero field, mismatch increases as f_g is tuned lower. This partially explains the reduction in gain with increasing field; in particular, in the higher Fraunhofer lobes, there is always a considerable impedance mismatch.

width w , the field B_L at which a vortex is stable is given by [49]

$$B_L = \frac{2\Phi_0}{\pi w^2} \ln\left(\frac{2w}{\pi\xi}\right) \simeq 2.4 \text{ mT}, \quad (\text{C29})$$

where we used the width w in Table I and the coherence length estimated above from the perpendicular critical field. The value is in agreement with the observed 2.4-mT hysteresis.

APPENDIX D: TWPA TRANSMISSION AND REFLECTION

As mentioned in Appendix B, the setup allowed measuring the TWPA transmission $|S_{21}|^2$ and the reflection $|S_{11}|^2$ using a circulator at the TWPA output. In the modeling above, we focus on the frequencies of TWPA features (f_g and f_p), and in the gain measurements, the calibration of the fridge lines is not so essential. This is partly because the setup to measure the TWPA in field was not particularly adapted to TWPA characterization experiments, where one would carefully calibrate the input and output lines to understand the insertion loss and dissipation inside the TWPA. Nonetheless, we have measured the TWPA's $|S_{21}|^2$ and $|S_{11}|^2$; see Figs. 9(a) and 9(b). The transmission and reflection input have nominally identical attenuation and the electrical losses in the TWPA are of the order of 4 dB, meaning that one can roughly compare $|S_{21}|^2$ and $|S_{11}|^2$. We see that close to the Fraunhofer minimum, where the transmission drops, the TWPA $|S_{11}|^2$ increases to similar levels as the maximum $|S_{21}|^2$ at low field. Thus we

can conclude that the TWPA mostly becomes reflective, as expected from the model.

Looking closer at the reflection data, we see smaller moving ripples in the TWPA reflection moving as a function of $B_{\parallel,1}$. They are also visible in the TWPA transmission, but reflection measurements are likely better for seeing small impedance mismatches. These ripples are likely due to standing waves between the TWPA input and output. As the magnetic field changes the inductance of the junction array, these standing waves shift.

We looked for signs of the TWPA becoming more dissipative for the B_{\perp} direction due to vortices in the JJ array or in the large bond pads at the input and output. To this end, we compared the transmission and reflection data as a function of B_{\perp} (not shown) with the data in Fig. 9. However, we also see a similar level of $|S_{11}|^2$ for regions where $|S_{21}|^2$ is already suppressed, meaning that the dominant effect with B_{\perp} is also just reflection due to mismatched impedance.

APPENDIX E: TWPA FIGURES OF MERIT AND THE OPTIMIZATION PROCEDURE

A TWPA is an amplifier; therefore, it has the usual figures of merit, e.g., gain, added noise (noise temperature or noise figure), bandwidth, and saturation power. For the scope of this work, we have focused on gain, bandwidth, gain fluctuations, and saturation power to understand how the TWPA changes with magnetic field. In this appendix we discuss how we measured them and how we optimized the gain at each field. The setup in the fridge with the magnet was not prepared to accurately measure the added

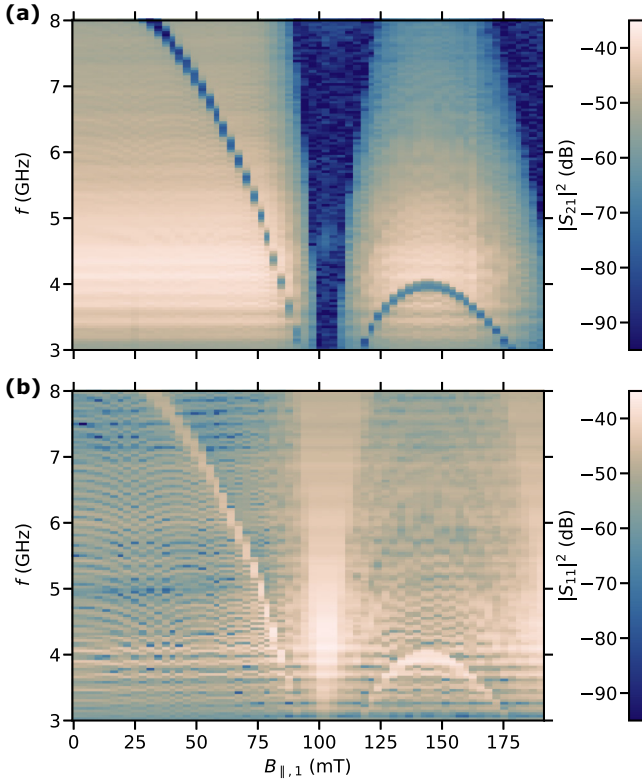


FIG. 9. TWPA transmission (a) and reflection (b) versus $B_{\parallel,1}$. It is apparent that, when the TWPA transmission is reduced at the Fraunhofer minimum, the reflection is enhanced and reaches similar levels.

noise of the TWPAs, but both TWPAs were characterized by Silent Waves before shipping, so we can give information about the added noise at zero magnetic field, which we discuss in the following.

In the factory calibration, the SNR improvement over a HEMT-amplifier-only configuration was measured, which can be used to estimate the added noise of the TWPAs. The optimized gain in the factory calibration is similar to the gain found in the Cologne setups at zero field with TWPA A in the magnet center, and with TWPA B inside the magnetic shields [see Figs. 10(a) and 10(c)]. Thus, the TWPA performance in the Cologne setups is likely similar. The factory SNR improvement for TWPAs A and B [Figs. 10(b) and 10(d)] is similar, but TWPA B shows smaller ripples, likely because the impedance matching is better. To make the SNR improvement meaningful, the noise temperature of the test setup ($T_{\text{noise}}^{\text{Setup}}$) without the TWPA needs to be estimated. The test setup uses a HEMT amplifier (LNF-LNC0.3_14B), which is specified to have $T_{\text{noise}} = 3.6$ K. With some additional losses in the setup, the measured noise temperature $T_{\text{noise}}^{\text{Setup}} \approx 5.7$ K is plausible [see Fig. 10(g) for data]. One can now look at the SNR improvement as a function of net gain, defined as gain corrected for insertion loss [see Fig. 10(f)]. This is shown in

Fig. 10(e) and it shows that TWPA B has a slightly better performance. The SNR improvement can be modeled as $a/(1 + a/G_{\text{TWPA}})$, where G_{TWPA} is the net gain of the TWPA and $a = T_{\text{noise}}^{\text{Setup}}/T_{\text{noise}}^{\text{TWPA}}$ is the ratio of the T_{noise} of the TWPA and the test setup without TWPA. We can roughly fit the data by setting $T_{\text{noise}}^{\text{Setup}}/T_{\text{noise}}^{\text{TWPA}} = 10$, which suggests that $T_{\text{noise}}^{\text{TWPA}} \approx 0.6$ K or an added noise level of about two photons. This is in line with more recent measurements of similar devices in the Silent Waves' test setup where the added noise was measured more directly. The TWPAs in this work thus operate slightly above the standard quantum limit.

While the added noise in the Cologne setups at zero field is likely similar to the factory calibration, we cannot exclude that both the magnetic field and temperature (see Appendix G) can introduce additional noise beyond the eventual reduction in gain. We did not measure the SNR improvement at different fields or temperatures, because such measurements would take significantly longer than the gain measurements. However, since we see the clear relation between SNR improvement and gain at zero field, and since we see no indication of increased TWPA noise with increasing field, the gain measurements at different fields are likely a good proxy for SNR improvement. The magnetic field and temperature are expected to introduce critical current noise, which will increase the added noise of the TWPA and small changes in the added noise might not be directly visible in the average gain curves. With a magnetic field, vortices might also be an additional noise source. While the reduction in gain that we see as a function of the magnetic field and temperature clearly shows that the TWPA is eventually compromised by both, we cannot exclude that the added noise is compromised even earlier. Measuring and understanding the added noise as a function of the temperature and magnetic field is an interesting future direction.

To estimate gain as a function of frequency, one would ideally do a full calibration of the setup and compare the $|S_{21}|^2$ with and without the optimized TWPA in the line. Our setup for the magnetic field dependence did not allow this and we did not take a calibration measurement without the TWPA that could be subtracted. There are different ways to still estimate the gain, but they have limitations. One can subtract the pump-off transmission from the pump-on transmission [cf. Fig. 1(d)]. However, since the pump moves the TWPA band gap (because it increases L_J), this would lead to artifacts. For TWPA A, we have instead taken the TWPA transmission spectra at different $B_{\parallel,1}$ within the first Fraunhofer lobe, which has the band gap at different frequencies, and taken the maximum at every frequency to estimate a background without a band gap [see Fig. 11(a)]. Taking the maximum at every frequency makes it less likely to overestimate the gain, but reflection at the TWPA input is likely subtracted from

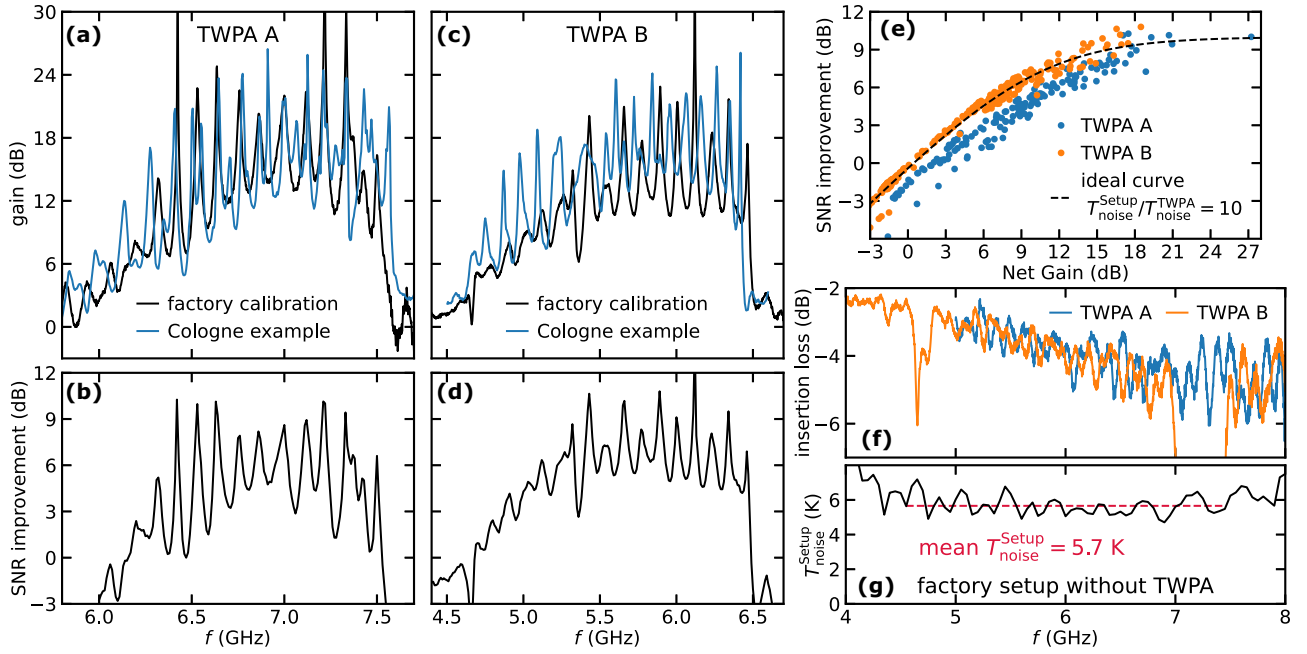


FIG. 10. Factory characterization data for TWPAs A and B and comparison with Cologne data. Panels (a) and (c) show the gain of the pumped over the unpumped TWPA, measured in the factory characterization as well as in the Cologne setup, for TWPAs A and B, respectively. Gain profiles are similar but not identical, likely due to impedance mismatches in the wider setup. (b),(d) SNR improvement of the TWPA over a TWPA bypass configuration for TWPAs A and B [for noise temperature of the setup without the TWPA, see (g)]. (e) SNR improvement versus net gain. Net gain computed based on pump-on versus pump-off gain minus TWPA insertion loss [see (f) for insertion loss].

the data as well. This is the background we subtracted to get the gain curves [see, for instance, Fig. 3(a)]. Crucially, we have always subtracted the same background, such that changes in the gain with magnetic field are relative to the same background. For TWPA B, which was mounted inside the magnetic shields, we could not move the band gap without compromising the TWPA; therefore, we just linearly interpolated the background in the band-gap region [see Fig. 11(b)], but also used the same background for all gain estimates.

With an established background to estimate the gain for each TWPA, we now describe the procedure to find the optimum P_{pump} and f_{pump} at different field settings. The gain generally shows strong ripples, likely due to impedance mismatches that could stem from deviations from the designed periodicity of the JJ array, reflections at the SMA connectors or the printed circuit board, box modes from the package, and, in the magnetic field measurements, our circulators being used at the edge of their specified range. The position of the ripples shifts with f_{pump} and P_{pump} , such that one could usually achieve 20 dB of gain at a specific frequency within the larger bandwidth window, but only at a more limited bandwidth of 30 MHz. For usual use cases, such as qubit readout, one could also directly optimize on the signal-to-noise ratio at a concrete frequency. However, for the field dependence we want to investigate, we decided that the optimum smooth gain

(maximum of the gain averaged in a 500-MHz window) would be a reasonable figure of merit to use as a cost function for optimization [see Fig. 3(a)]. So at every field we ran a Nelder-Mead optimization [37] of the maximum smooth gain using f_{pump} and P_{pump} as optimization parameters. The optimization usually converged with a median of 24 iterations and was not very sensitive to initial conditions. Other figures of merit are conceivable, e.g., one could define a figure of merit that penalizes gain fluctuations or one could optimize on the SNR improvement or, with a precise setup calibration, even on the mean added noise. Our choice, the smoothed gain, is simple, can be measured quickly, and allows for the definition of a robust 3-dB bandwidth. Given that we used the same optimization at every magnetic field, we believe that the optimum smooth gain offers a good way to evaluate the TWPA performance as a function of the field.

We can now compare the three different field directions. In Figs. 3(b), 4(d), and 4(e), the gain was plotted as a function of the respective field strength; by looking at the gain and bandwidth as a function of f_g , we show that even for the same f_g , which tunes differently with $B_{\parallel,1}$, $B_{\parallel,2}$, and B_{\perp} , the TWPA performance differs strongly; see Figs. 12(a) and 12(b). The only field direction for which the gain stays high over an extended field range is $B_{\parallel,1}$, as expected. For $B_{\parallel,2}$, the band gap closes and reopens, which compromises the phase matching, causing reduced gain, while, for B_{\perp} ,

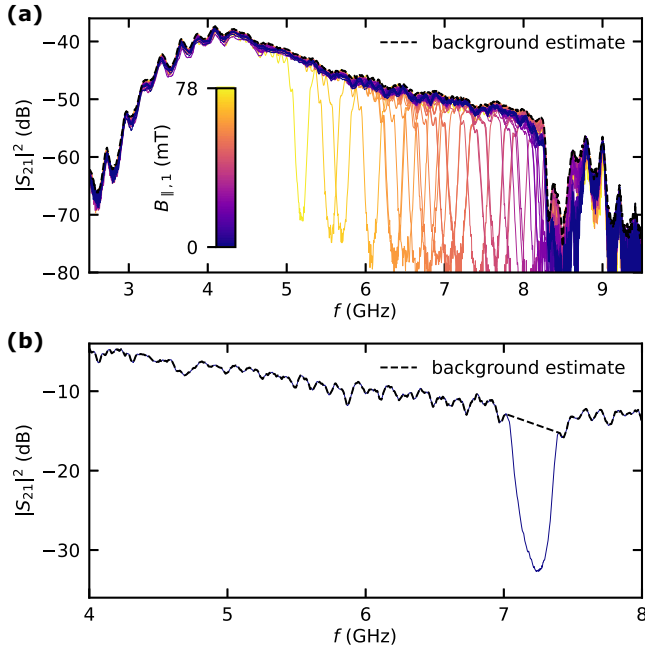


FIG. 11. TWPA transmission spectrum for different $B_{\parallel,1}$ (colored lines). The data are taken from the main Fraunhofer lobe. The circulators are specified in the 4–8 GHz range, which is clearly visible in $|S_{21}|^2$. We take the maximum $|S_{21}|^2$ at every frequency to estimate a background (black line) that we use for subtraction in the gain estimation. This background will more likely underestimate than overestimate the gain.

likely vortices lead to the strong dissipation. The TWPA bandwidth is eventually reduced even for $B_{\parallel,1}$; the outliers in the bandwidth at high fields have much lower maximum gain, which makes a larger bandwidth easier.

To understand the TWPA tune-up for a changing f_g , we also show the difference between the pump frequency and gap frequency $f_g - f_{\text{pump}}$ and pump power P_{pump} , obtained by optimizing the maximum smooth gain at every field; see Figs. 12(c) and 12(d). We find that at low fields (high f_g) the optimum f_{pump} is slightly further away from the center of the band gap and it moves a bit closer as the fields tune down f_g . The pump power P_{pump} is specified as the power set on the microwave source, not at the input of the TWPA. The installed attenuation between the fridge input and the TWPA is 60 dB with additional attenuation due to cable and component losses and reflections. For P_{pump} , there appears to be a clear linear relationship between the optimum P_{pump} and f_g independent of the field direction. Intuitively, this is expected because the field reduces the critical current I_c of the JJs and hence the optimum P_{pump} , as well as the saturation power of the TWPA. At several fields, we also took measurements to estimate the 3-dB saturation power, and found that it is consistently about 20 dB below P_{pump} . We generally measured the gain with a VNA signal power of –30 dBm. The signal power approaches

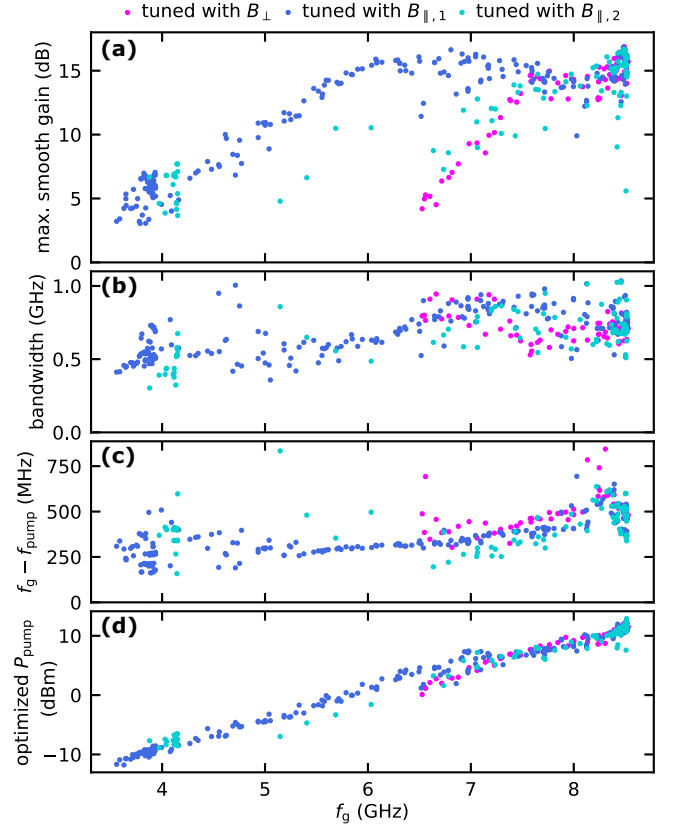


FIG. 12. TWPA figures of merit as a function of the estimated f_g for $B_{\parallel,1}$, $B_{\parallel,2}$, and B_{\perp} . The f_g tuning is different for all field directions, but this figure shows that f_g alone does not determine performance. Panel (a) shows that the gain varies widely even for the same f_g , while the bandwidth in (b) does not change dramatically. Panels (c) and (d) show that the optimum P_{pump} and optimum f_{pump} are mainly a function of f_g and mostly independent of the field direction. The saturation power was measured for a number of field strengths and directions, and was consistently about 20 dB below P_{pump} .

saturation power levels only for the lowest f_g , where the gain is already severely compromised.

APPENDIX F: SETUP AND FIELD DEPENDENCE FOR THE SHIELDED TWPA

In this appendix, we describe the mounting of the TWPA with magnetic shielding and cryogenic switches that allow bypassing the device. This setup then allows flexible use of the TWPA when needed up to the fields allowed by the shielding. The setup is illustrated in Fig. 13. Figure 13(a) shows a photograph of the fridge with the TWPA mounted above the mixing chamber plate and the magnet and sample positions indicated. From the datasheet of the magnet, we can estimate the stray field at the TWPA position: at 1 T, the stray field would already be of the order of 5 mT, enough to severely compromise the TWPA. The stray field for 6 T at the sample as a function of the distance

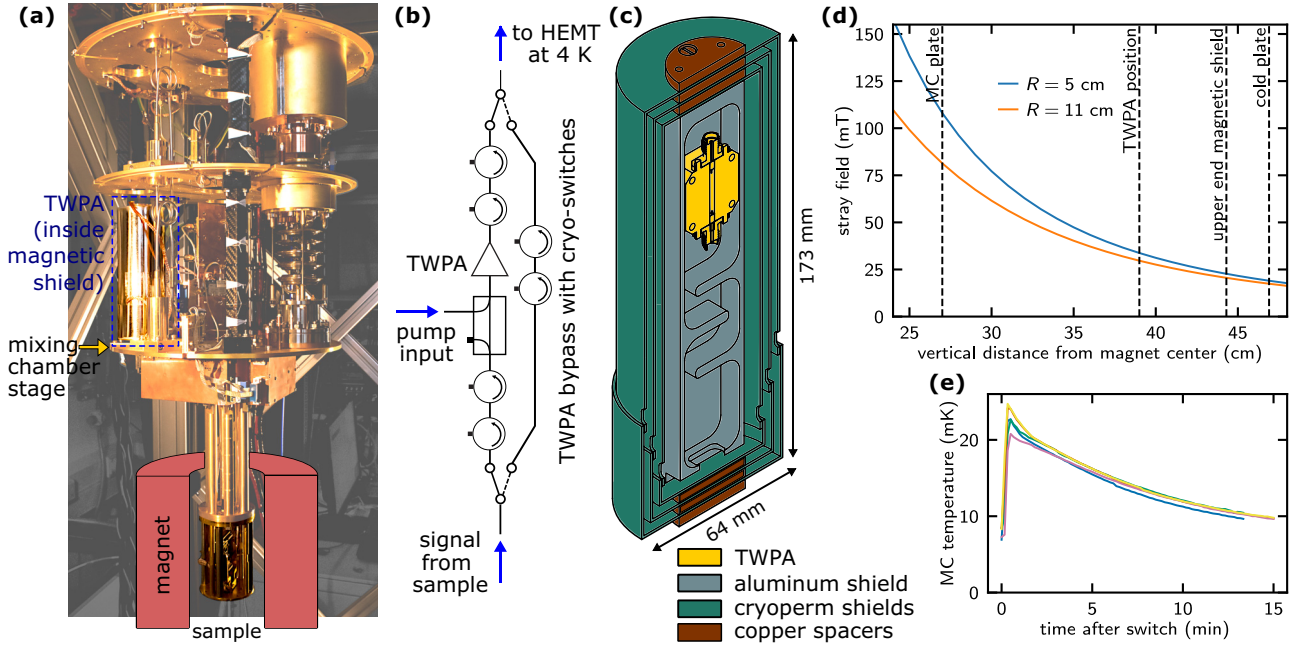


FIG. 13. (a) Fridge photograph and wiring diagram of the TWPA. The TWPA inside the magnetic shields is mounted above the mixing chamber. It is sandwiched between two double-junction isolators (LNF-ISISC4_12A) for protection from electrostatic discharge. Two two-way switches (single pole, double throw) (Radiall R571433141) were integrated into the wiring such that the TWPA can be bypassed. The bypass line has a separate set of circulators. (b) Circuit diagram of the switch setup. (c) Colorized technical drawing of the magnetic shields and TWPA. Three cylindrical cryoperm shields of 1-mm strength are used. (d) Stray field of the B_z magnet at 6 T as a function of the vertical distance from the center of the magnet for different radial distances approximately corresponding to inner and outer shield boundaries. TWPA position and fridge stages are marked by dashed black lines. (e) MC temperature as a function of time after a switch event, measured several times to show consistency.

is shown in Fig. 13(d). Instead of using only passive magnetic fields, one could also use an additional compensation coil to cancel the stray field at the position of the TWPA [25].

With these stray fields in mind, we contacted a company to make a mu-metal-like shielding setup for the TWPA. A schematic of the shields is shown in Fig. 13(c). We chose three layers of 1-mm-thick Cryoperm—an iron-nickel alloy that undergoes special treatment. As an inner shield, we chose an aluminum box, which should act as a perfect diamagnet up to the critical field of bulk aluminum of around 10 mT. The shields have holes for the two coaxial cables for the TWPA input and output and for a copper braid that is used to thermally anchor the TWPA inside the shields directly to the mixing chamber. Given that we have a bottom-loading fridge that is used for other experiments as well, it is crucial that the magnetic shields are not compromised by sweeping the field to 6 T because it would have meant opening the fridge to remove the shields and TWPA in case higher fields would be needed.

To preserve different functionalities in the fridge, we also installed current-operated cryogenic switches that allow bypassing the TWPA. This is useful, as the TWPA does not work at high fields, and because it only gives a signal-to-noise improvement in a frequency range that

is narrow compared to the HEMT. Also, when it is not pumped, it adds frequency-dependent attenuation to the line, as is evident from the ripples in the pump-off transmission figures. The wiring diagram is shown in Fig. 13(b). There are isolators (model LNF-ISISC4_12A) between the switches and the TWPA on both sides that provide a low-impedance path to ground and protect the high-impedance TWPA from electrostatic discharge. Both the bottom loading as well as the switching could otherwise be dangerous to the TWPA. By testing both, we confirmed that the TWPA is safe in this configuration. We found a good current and time for reliable switching that does not raise the mixing chamber temperature much. Several example curves of the mixing chamber temperature as a function of time after switching events are shown in Fig. 13(e). The temperature generally stays below 25 mK and the base temperature is reached again after about 20 min. Success of switching was confirmed each time.

Sufficiently high magnetic fields can also be a problem for the circulators and isolators that could influence TWPA performance via impedance mismatches. Contrary to the Quinstar circulators used in the measurements with the TWPA at the magnet center (see Appendix B) and for the TWPA bypass path (see Fig. 13), the LNF isolators on either side of the TWPA have only a single layer

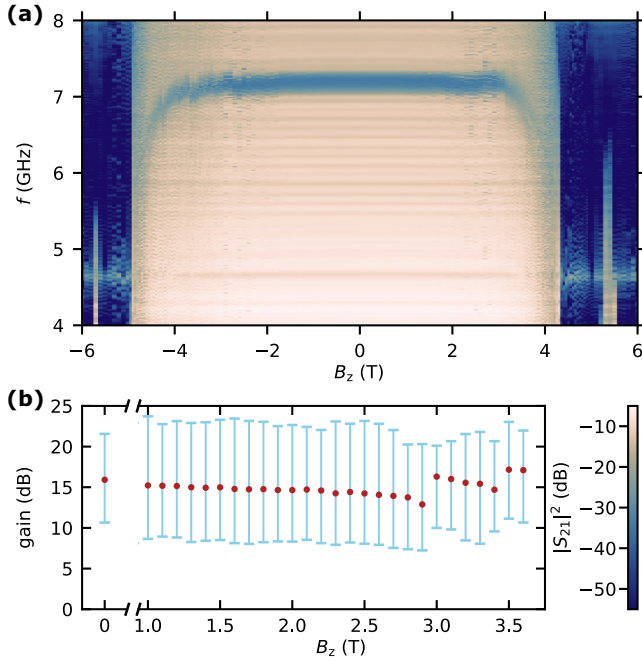


FIG. 14. (a) TWPA $|S_{21}|^2$ as a function of the field swept from 6 to -6 T for the shielded TWPA. There is strong hysteresis in the data, likely originating from the magnetic shields. (b) TWPA maximum smooth gain and gain range in the 3-dB-bandwidth window at high fields. Here, f_{pump} and P_{pump} were optimized at higher fields.

of magnetic shields. These shields will likely be compromised around 2 T at the magnet, at which point the TWPA shields are also starting to fail (see Fig. 14). However, the isolators themselves are specified to not be compromised by magnetic fields up to 65 mT (the manufacturer states that the magnetic shields fail before the devices themselves do), and they are mounted above the mixing chamber plate at a similar height as the TWPA. Thus, according to our stray field estimates [Fig. 13(d)], the isolators will only get close to the specified limit around the maximum field of our magnet, 6 T, far beyond the point where the TWPA is compromised. We can thus conclude that the field compatibility of the isolators is not an important factor in our experiment.

In the main text, $|S_{21}|^2$ data for the shielded TWPA are only shown up to 3.5 T and f_{gap} starts to drop significantly for $B_z > 2.5$ T (see Fig. 5). We did not sweep the field to 6 T right away, because we were initially worried that at the highest fields, the magnetic shields might be magnetized, which would not be reversible while they remain inside the dilution refrigerator. However, ultimately, we swept the magnetic field over the maximum range. The TWPA $|S_{21}|^2$ as a function of B_z for the downsweep from 6 to -6 T is shown in Fig. 14(a). It is evident that the TWPA transmission breaks down relatively suddenly for the highest fields and that there is hysteresis of the order

of 0.5 T. The f_g exhibits a plateau between approximately 2 and -2 T. From the stray field data [Fig. 13(d)], we can estimate the stray field at the TWPA position for 2 T at the magnet center to be approximately 11 mT if the shields were not present. Outside it shows the expected reduction with the field, but also some jumps in particular between -2 and -4 T. We possibly see a Fraunhofer lobe both at positive and negative fields. The field direction is likely a superposition of $B_{\parallel,2}$ and B_{\perp} in the TWPA coordinate system. While the hysteresis and sudden breakdown of $|S_{21}|^2$ are reminiscent of the B_{\perp} dataset of the unshielded TWPA, both the sudden breakdown and hysteresis are likely due to the magnetic shields.

For the gain measurement as a function of B_z for the shielded TWPA, shown in Fig. 5(b), we did not adapt f_{pump} and P_{pump} , because we were interested in the performance of the TWPA in the most straightforward mode of operation. Figure 14(b) shows additional data, where it was attempted to optimize f_{pump} and P_{pump} at higher fields. A good f_{pump} guess and a corresponding P_{pump} can usually be based on f_g , but above 3 T the band gap becomes less visible and slightly above 3.5 T no good gain could be realized. However, in the unpumped $|S_{21}|^2$, there is already more noise visible above 2 T and this also shows up in the gain curves, leading to visibly more added noise. We would therefore conclude that the valid operating window for the TWPA in our setup is roughly -2 to 2 T.

APPENDIX G: TWPA TEMPERATURE DEPENDENCE

We investigate here the temperature dependence of the TWPA response. If the TWPA could be mounted at a higher, warmer temperature stage of the fridge, that would increase the distance to the magnet and decrease the stray field [see Fig. 13(d)]. Data of the TWPA transmission and optimized gain as a function of temperature are shown in Fig. 15. Different temperatures were stabilized using a proportional-integral-derivative controller on the mixing chamber heater with the mixing chamber temperature as the signal. We stabilized each temperature for about 10 min to ensure thermalization of the TWPA and rejected datasets where temperature fluctuations were too high.

Apart from mounting the TWPA away from a magnet, the temperature dependence is interesting to compare to the magnetic field dependence, because both suppress the superconducting gap. For a BCS superconductor such as aluminum, a good approximation (within less than 2%) for the temperature-dependent gap is [50]

$$\Delta(T) = \Delta(0) \tanh(1.74\sqrt{T_c/T - 1}), \quad (\text{G1})$$

where we estimate the critical temperature $T_c = 1.27$ K based on the thicker 50-nm aluminum film that would have the smaller T_c [51]. Using this gap dependence and

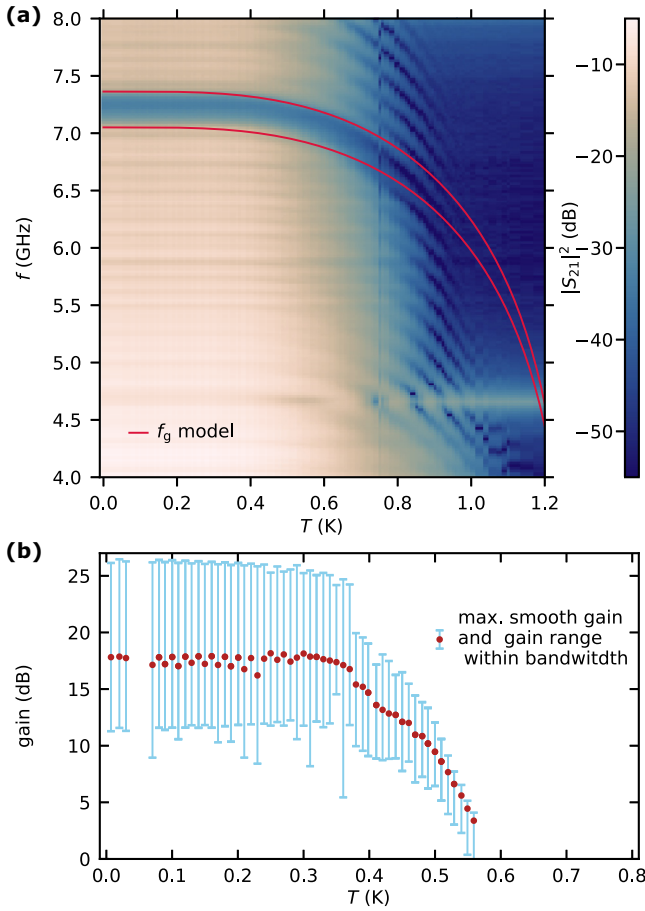


FIG. 15. (a) Temperature dependence of the TWPA transmission. The band gap is modeled using the TWPA-B parameters in Table I, and a temperature-dependent gap based on Eq. (G1) with $T_c = 1.27$ K. (c) Best values for optimized maximum smooth gain at different temperatures. The error bars show the maximum and minimum gains inside the 3-dB bandwidth. Up to 0.3 K there is no strong temperature dependence, neither for the transmission nor for the maximum gain.

the TWPA-B parameters from Table I, we can model the temperature dependence of f_g analogous to the field dependence described in Appendix C. Data and the model are shown in Fig. 15(a). The model describes the evolution of f_g well up to about 0.6 K. For higher temperatures, the band gap fades as overall transmission is suppressed. Instead of $|S_{21}|^2$ showing a clear boundary as f_p is reduced with T , which is the case for the magnetic field dependence, $|S_{21}|^2$ instead develops ripples that move down with temperature.

Up to 0.3 K, the almost unchanged $|S_{21}|^2$ and gain suggests that the TWPA is not strongly compromised, but we did not explicitly measure the added noise at each temperature. Given that the TWPA added noise is likely of the order of 0.6 K, it is not implausible that raising the device temperature at first does not increase the added noise too much. However, we do not claim that the TWPA has the same performance at 0.3 K as at base temperature, just

that our measurement of gain and device transmission do not show a difference. We conclude that one could likely mount the TWPA at the cold plate of the dilution refrigerator that is at 0.1 K. This could increase the distance to the magnet and likely at least double the maximum field at which the TWPA can be operated without adding more shielding.

- [1] M. Esposito, A. Ranadive, L. Planat, and N. Roch, Perspective on traveling wave microwave parametric amplifiers, *Appl. Phys. Lett.* **119**, 120501 (2021).
- [2] C. Macklin, K. O'Brien, D. Hover, M. E. Schwartz, V. Bolkhovskoy, X. Zhang, W. D. Oliver, and I. Siddiqi, A near-quantum-limited Josephson traveling-wave parametric amplifier, *Science* **350**, 307 (2015).
- [3] L. Planat, A. Ranadive, R. Dassonneville, J. Puertas Martínez, S. Léger, C. Naud, O. Buisson, W. Hasch-Guichard, D. M. Basko, and N. Roch, Photonic-crystal Josephson traveling-wave parametric amplifier, *Phys. Rev. X* **10**, 021021 (2020).
- [4] B. Ho Eom, P. Day, H. LeDuc, and J. Zmuidzinas, A wideband, low-noise superconducting amplifier with high dynamic range, *Nat. Phys.* **8**, 623 (2012).
- [5] S. Goldstein, N. Kirsh, E. Svetitsky, Y. Zamir, O. Hachmo, C. E. M. de Oliveira, and N. Katz, Four wave-mixing in a microstrip kinetic inductance travelling wave parametric amplifier, *Appl. Phys. Lett.* **116**, 152602 (2020).
- [6] M. Malnou, M. Vissers, J. Wheeler, J. Aumentado, J. Hubmayr, J. Ullom, and J. Gao, Three-wave mixing kinetic inductance traveling-wave amplifier with near-quantum-limited noise performance, *PRX Quantum* **2**, 010302 (2021).
- [7] S. Shu, N. Klimovich, B. H. Eom, A. D. Beyer, R. B. Thakur, H. G. Leduc, and P. K. Day, Nonlinearity and wide-band parametric amplification in a (Nb, Ti)N microstrip transmission line, *Phys. Rev. Res.* **3**, 023184 (2021).
- [8] A. Ranadive, M. Esposito, L. Planat, E. Bonet, C. Naud, O. Buisson, W. Guichard, and N. Roch, Kerr reversal in Josephson meta-material and traveling wave parametric amplification, *Nat. Commun.* **13**, 1737 (2022).
- [9] F. Luthi, T. Stavenga, O. W. Enz, A. Bruno, C. Dickel, N. K. Langford, M. A. Rol, T. S. Jespersen, J. Nygård, P. Krogstrup, and L. DiCarlo, Evolution of nanowire transmon qubits and their coherence in a magnetic field, *Phys. Rev. Lett.* **120**, 100502 (2018).
- [10] A. Schneider, T. Wolz, M. Pflümann, M. Spiecker, H. Rotzinger, A. V. Ustinov, and M. Weides, Transmon qubit in a magnetic field: Evolution of coherence and transition frequency, *Phys. Rev. Res.* **1**, 023003 (2019).
- [11] M. Pita-Vidal, A. Bargerboos, C.-K. Yang, D. J. van Woerkom, W. Pfaff, N. Haider, P. Krogstrup, L. P. Kouwenhoven, G. de Lange, and A. Kou, Gate-tunable field-compatible fluxonium, *Phys. Rev. Appl.* **14**, 064038 (2020).
- [12] A. Kringhøj, T. W. Larsen, O. Erlandsson, W. Uilhoorn, J. G. Kroll, M. Hesselberg, R. P. G. McNeil, P. Krogstrup, L. Casparis, C. M. Marcus, and K. D. Petersson, Magnetic-field-compatible superconducting transmon qubit, *Phys. Rev. Appl.* **15**, 054001 (2021).

- [13] J. Krause, C. Dickel, E. Vaal, M. Vielmetter, J. Feng, R. Bounds, G. Catelani, J. M. Fink, and Y. Ando, Magnetic field resilience of three-dimensional transmons with thin-film Al/AIO_x/Al Josephson junctions approaching 1 T, *Phys. Rev. Appl.* **17**, 034032 (2022).
- [14] A. Bienfait, J. J. Pla, Y. Kubo, M. Stern, X. Zhou, C. C. Lo, C. D. Weis, T. Schenkel, M. L. W. Thewalt, D. Vion, D. Esteve, B. Julsgaard, K. Mølmer, J. J. L. Morton, and P. Bertet, Reaching the quantum limit of sensitivity in electron spin resonance, *Nat. Nanotechnol.* **11**, 253 (2016).
- [15] Z. Wang, L. Balembois, M. Rančić, E. Billaud, M. Le Dantec, A. Ferrier, P. Goldner, S. Bertaina, T. Chanelière, D. Esteve, D. Vion, P. Bertet, and E. Flurin, Single-electron spin resonance detection by microwave photon counting, *Nature* **619**, 276 (2023).
- [16] W. Vine, A. Kringhøj, M. Savitskyi, D. Parker, T. Schenkel, B. C. Johnson, J. C. McCallum, A. Morello, and J. J. Pla, Latched detection of zeptojoule spin echoes with a kinetic inductance parametric oscillator, *Sci. Adv.* **10**, eadm7624 (2024).
- [17] S. Schaal, I. Ahmed, J. A. Haigh, L. Hutin, B. Bertrand, S. Barraud, M. Vinet, C.-M. Lee, N. Stelmashenko, J. W. A. Robinson, J. Y. Qiu, S. Hacoen-Gourgy, I. Siddiqi, M. F. Gonzalez-Zalba, and J. J. L. Morton, Fast gate-based readout of silicon quantum dots using Josephson parametric amplification, *Phys. Rev. Lett.* **124**, 067701 (2020).
- [18] D. de Jong, C. G. Prosko, D. M. A. Waardenburg, L. Han, F. K. Malinowski, P. Krogstrup, L. P. Kouwenhoven, J. V. Koski, and W. Pfaff, Rapid microwave-only characterization and readout of quantum dots using multiplexed gigahertz-frequency resonators, *Phys. Rev. Appl.* **16**, 014007 (2021).
- [19] M. Aghaee, A. A. Ramirez, Z. Alam, R. Ali, M. Andrzejczuk, A. Antipov, M. Astafev, A. Barzegar, B. Bauer, J. Becker *et al.*, Interferometric single-shot parity measurement in an InAs-Al hybrid device, [arXiv:2401.09549](https://arxiv.org/abs/2401.09549).
- [20] M. Kounalakis, Y. M. Blanter, and G. A. Steele, Flux-mediated optomechanics with a transmon qubit in the single-photon ultrastrong-coupling regime, *Phys. Rev. Res.* **2**, 023335 (2020).
- [21] T. Bera, S. Majumder, S. K. Sahu, and V. Singh, Large flux-mediated coupling in hybrid electromechanical system with a transmon qubit, *Commun. Phys.* **4**, 12 (2021).
- [22] Y. Tabuchi, S. Ishino, A. Noguchi, T. Ishikawa, R. Yamazaki, K. Usami, and Y. Nakamura, Coherent coupling between a ferromagnetic magnon and a superconducting qubit, *Science* **349**, 405 (2015).
- [23] M. Kounalakis, G. E. W. Bauer, and Y. M. Blanter, Analog quantum control of magnonic cat states on a chip by a superconducting qubit, *Phys. Rev. Lett.* **129**, 037205 (2022).
- [24] C. Bartram *et al.*, Dark matter axion search using a Josephson traveling wave parametric amplifier, *Rev. Sci. Instrum.* **94**, 044703 (2023).
- [25] R. Di Vora *et al.* (QUAX Collaboration), Search for galactic axions with a traveling wave parametric amplifier, *Phys. Rev. D* **108**, 062005 (2023).
- [26] M. Xu, R. Cheng, Y. Wu, G. Liu, and H. X. Tang, Magnetic field-resilient quantum-limited parametric amplifier, *PRX Quantum* **4**, 010322 (2023).
- [27] M. Khalifa and J. Salfi, Nonlinearity and parametric amplification of superconducting nanowire resonators in magnetic field, *Phys. Rev. Appl.* **19**, 034024 (2023).
- [28] A. Vaartjes, A. Kringhøj, W. Vine, T. Day, A. Morello, and J. J. Pla, Strong microwave squeezing above 1 tesla and 1 kelvin, *Nat. Commun.* **15**, 4229 (2024).
- [29] L. J. Splitthoff, J. J. Wesdorp, M. Pita-Vidal, A. Bargerbos, Y. Liu, and C. K. Andersen, Gate-tunable kinetic inductance parametric amplifier, *Phys. Rev. Appl.* **21**, 014052 (2024).
- [30] S. Frasca, C. Roy, G. Beaulieu, and P. Scarlino, Three-wave-mixing quantum-limited kinetic inductance parametric amplifier operating at 6 T near 1 K, *Phys. Rev. Appl.* **21**, 024011 (2024).
- [31] N. Zapata, I. Takmakov, S. Günzler, A. Nambisan, D. Rieger, T. Reisinger, W. Wernsdorfer, and I. M. Pop, Granular aluminum parametric amplifier for low-noise measurements in tesla fields, [arXiv:2403.10669](https://arxiv.org/abs/2403.10669).
- [32] W. Uilhoorn, J. G. Kroll, A. Bargerbos, S. D. Nabi, C.-K. Yang, P. Krogstrup, L. P. Kouwenhoven, A. Kou, and G. de Lange, Quasiparticle trapping by orbital effect in a hybrid superconducting-semiconducting circuit, [arXiv:2105.11038](https://arxiv.org/abs/2105.11038).
- [33] V. Elhomsy, L. Planat, D. J. Niegemann, B. Cardoso-Paz, A. Badreldin, B. Klemm, V. Thiney, R. Lethiecq, E. Eyraud, M. C. Dartailh, B. Bertrand, H. Niebojewski, C. Bäuerle, M. Vinet, T. Meunier, N. Roch, and M. Urdampilleta, Broadband parametric amplification for multiplexed SiMOS quantum dot signals, [arXiv:2307.14717](https://arxiv.org/abs/2307.14717).
- [34] A. Abrikosov and L. Gor'kov, Contribution to the theory of superconducting alloys with paramagnetic impurities, *Soviet Phys. JETP* **12**, 1243 (1961).
- [35] S. Skalski, O. Betbeder-Matibet, and P. R. Weiss, Properties of superconducting alloys containing paramagnetic impurities, *Phys. Rev.* **136**, A1500 (1964).
- [36] F. Lecocq, I. M. Pop, Z. Peng, I. Matei, T. Crozes, T. Fournier, C. Naud, W. Guichard, and O. Buisson, Junction fabrication by shadow evaporation without a suspended bridge, *Nanotechnology* **22**, 315302 (2011).
- [37] J. A. Nelder and R. Mead, A simplex method for function minimization, *Comput. J.* **7**, 308 (1965).
- [38] A. Barone and G. Paternò, *Physics and Applications of the Josephson Effect* (Wiley, New York, 1982).
- [39] R. Kuzmin, N. Mehta, N. Grabon, and V. E. Manucharyan, Tuning the inductance of Josephson junction arrays without SQUIDs, *Appl. Phys. Lett.* **123**, 182602 (2023).
- [40] J. H. Nielsen *et al.*, Qcodes/qcodes: Qcodes 0.43.0 (2024), <https://doi.org/10.5281/zenodo.596989>.
- [41] M. A. Rol, C. Attryde, J. C. van Oven, K. Loh, J. Gludemans, V. Negîrneac, T. Last, and C. C. Bultink, in *APS March Meeting Abstracts* (2021), Vol. 2021, p. M34–001. <https://zenodo.org/records/10728283>.
- [42] <https://zenodo.org/records/10728283>.
- [43] A. Barone, G. Paternò, M. Russo, and R. Vaglio, Diffraction and interference phenomena in single Josephson junctions, *Physica Status Solidi (a)* **41**, 393 (1977).
- [44] K. Maki, in *Superconductivity* (Routledge, 2018), p. 1035.
- [45] G. Catelani, X. S. Wu, and P. W. Adams, Fermi-liquid effects in the gapless state of marginally thin superconducting films, *Phys. Rev. B* **78**, 104515 (2008).

- [46] P. W. Adams, H. Nam, C. K. Shih, and G. Catelani, Zeeman-limited superconductivity in crystalline Al films, [Phys. Rev. B **95**, 094520 \(2017\)](#).
- [47] D. López-Núñez, Q. P. Montserrat, G. Rius, E. Bertoldo, A. Torras-Coloma, M. Martínez, and P. Forn-Díaz, Magnetic penetration depth of aluminum thin films, [arXiv:2311.14119](#).
- [48] M. Tinkham, *Introduction to Superconductivity* (Dover Publications, Mineola, NY, USA, 2004), 2nd ed.
- [49] K. H. Kuit, J. R. Kirtley, W. van der Veur, C. G. Moleenaar, F. J. G. Roesthuis, A. G. P. Troeman, J. R. Clem, H. Hilgenkamp, H. Rogalla, and J. Flokstra, Vortex trapping and expulsion in thin-film $\text{YBa}_2\text{Cu}_3\text{O}_{7-\delta}$ strips, [Phys. Rev. B **77**, 134504 \(2008\)](#).
- [50] F. Gross, B. S. Chandrasekhar, D. Einzel, K. Andres, P. J. Hirschfeld, H. R. Ott, J. Beuers, Z. Fisk, and J. L. Smith, Anomalous temperature dependence of the magnetic field penetration depth in superconducting UBe_{13} , [Z. Physik B - Condens. Matter **64**, 175 \(1986\)](#).
- [51] G. Marchegiani, L. Amico, and G. Catelani, Quasiparticles in superconducting qubits with asymmetric junctions, [PRX Quantum **3**, 040338 \(2022\)](#).